A Complete Breast Cancer Detection Approach Via Quantitative and Qualitative Analysis of Breast Ultrasound (BUS) Images

By

AMK Muntasir Shamim	Student ID – 142407
Mohmmad Ebne Enayet	Student ID – 142448
Ehsan Abir	Student ID - 142461

A thesis submitted to Islamic University of Technology

B.Sc. in Electrical and Electronic Engineering

Supervisor

Prof. Dr. Md Ruhul Amin
Professor
Department of EEE, IUT, Board Bazar, Gazipur-1704.

Certificate of Approval

The thesis titled “A Complete Breast Cancer Detection Approach Via Quantitative and Qualitative Analysis of Breast Ultrasound (BUS) Images.” submitted by AMK Muntasir Shamim, Mohammad Ebne Enayet, Ehsan Abir bearing student ID 142407,142448 ,142461 respectively of Academic Year 2017-2018 has been found as satisfactory and accepted as partial fulfillment of the requirement for the degree of Bachelor of Science in Electrical and Electronic Engineering on, 2017.

Dr. Md Ruhul Amin (Supervisor)
Professor
Department of Electrical and Electronic Engineering
Islamic University of Technology
Board Bazar, Gazipur-1704, Bangladesh.

Dedication

This thesis is dedicated to our beloved parents and all our well-wishers helping us to accomplish this work.

Acknowledgment

First of all, we would like express my heartiest gratitude to the Almighty Allah for providing us the strength to complete this thesis work. After the Almighty, it is my great pleasure to express gratitude to the people who made this thesis possible.

Foremost, I would like to express my deepest gratitude to my supervisor, Prof. Dr. Ruhul Amin, PhD, Dept. of EEE, IUT whose expertise, understanding and patience, added significantly to my graduate experience. This study could have never been done without my supervisors' motivation, guidance and inspiration.

We would also like to thank our mentor and Co-supervisor Dr. S. Kaisar Alam, Adjunct Professor, Rutgers University, NJ who sacrificed his valuable time for continuously guiding and motivating us for completing the thesis. He taught us how to work with the medical ultrasound imaging system and introduced me with the philosophical aspect of research which I will carry with me for the rest of my life.

We would like to acknowledge Dr. Juan Shan, Assistant Professor, Pace University, NY, USA, Prof. Dr. Dimitris Metaxas, Professor, Rutgers University, NJ, USA and Dr. Brian S. Garra. M.D., FDA, Silver Spring, MAD, USA for a number of stimulating discussions on the thesis. They enriched my understandings regarding the topic by sharing their valuable knowledge.

I would like express my heartfelt gratitude to Prof. Dr. Md. Ashraful Hoque, Head, Dept. of EEE. I would like to thank all the faculty members of EEE Dept., IUT for their continuous support and encouragement.

Abstract

Globally, cancer is becoming a major health issue as advances in modern medicine continue to extend the human life span. In the U.S., cancer is the second most-common cause of death, exceeded only by heart disease and accounting for nearly one of every four deaths. Breast cancer ranks second as a cause of cancer death in women (after lung cancer).

Thus, early detection and treatment are critical in reducing breast cancer related mortality. Working with Breast ultrasound (BUS) data or image is regarded as a challenging task due to the inherent nature of ultrasound imaging. Ultrasound imaging is characterized by speckle patterns, anisotropy and signal drop-out. Moreover, proper image acquisition techniques by the clinicians and their level of expertise also play a dominant role in determining the image quality. The fuzziness in the shape and boundaries of the breast lesions make it very difficult to automate the segmentation of BUS images. In order to improve the issues prevalent in the existing approaches, a complete qualitative and quantitative analysis of Breast ultrasound (BUS) images is proposed in this thesis. The method involves three steps – (a) Strain imaging by means of strain estimation, (b) Final Segmentation of the detected lesion and (c) Quantitative analysis of the lesion.

Contents

1 Introduction

1.1 Breast Cancer Scenario

Breast cancer is the most common and the second-most lethal cancer among females worldwide [1]. Among the women only in USA, breast cancer alone is expected to account for 29% of all the new cancer diagnoses with an estimate of 246,660 cases in 2016 [2]. Breast cancer survival rates vary greatly worldwide, ranging from 80% or over in North America, Sweden and Japan to around 60% in middle-income countries and below 40% in low-income countries [3]. Statistics reveals that if breast cancer is diagnosed at a localized stage then the 5-year relative survival rate approaches to 99% [4]. Since the causes of breast cancer still remain unknown, early detection and treatment of breast cancer is the top most priority in reducing breast cancer related mortality.

1.2 Medical Imaging in Breast Cancer Detection

Current methods for detecting and diagnosing breast cancer includes mammography, ultrasound imaging and magnetic resonance imaging (MRI). In this section, the standard imaging modalities for early detection of breast cancer is discussed.

1.2.1 Mammography

Mammography is specialized medical imaging that uses a low-dose x-ray system to see inside the breasts. This is considered as the standard imaging method for earlier detection and diagnosis of breast cancer [5, 6]. Two schemes of mammography is used in breast cancer detection and diagnosis namely Screening Mammography and Diagnostic Mammography. Typically, the first step in breast cancer detection is screening mammography which is a

low-dose X-ray examination on asymptomatic women. Diagnostic mammography is an X-ray examination done to evaluate a breast complaint or to investigate an abnormality found during a physical examination or during screening mammography. A typical breast mammogram is shown in Figure 1-1.

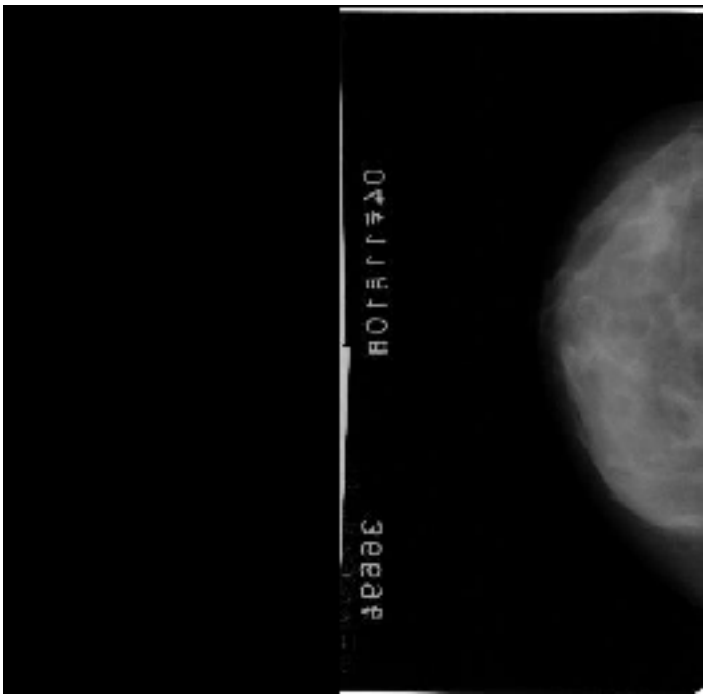

Figure 1-1 A typical breast mammogram (Image courtesy: Radiological Society of North America)

However, mammography suffers from different limitations such as low specificity of in case of adolescent women with dense breast [5] and potential risk towards patients' health due to ionizing radiation [7]. Many unnecessary (65–85%) biopsy operations are due to the low specificity of mammography. The unnecessary biopsies not only increase the cost, but also cause emotional suffering for the patients.

1.2.2 Magnetic Resonance Imaging (MRI)

Magnetic resonance imaging is a medical imaging technique used in radiology to investigate the anatomy and physiology of the body during both health and disease states. MRI scanners employ magnetic fields and radio waves to form images of the body. The technique is widely used in hospitals for medical diagnosis and, the staging of diseases and to perform follow-ups without causing exposure to ionizing radiation. A real MRI scanner is shown Figure 1-2.

Figure 1-2 An illustration of a real MRI scanner

Breast MRI has a number of different uses for breast cancer, including:

- Screening high-risk women (women known to be at higher than average risk for breast cancer, either because of a strong family history or a gene abnormality)
- Gathering more information about an area of suspicion found on a mammogram or ultrasound
- Monitoring for recurrence after treatment

Although breast MRI is a more sensitive test than mammography in many ways, this increased sensitivity may cause areas of the breast that do not have cancer to appear abnormal, producing an increased number of false-positive test results. False-positive test results indicate cancer when no cancer is actually present. A breast MRI with false positive nodule is illustrated in Figure 1-3. This false-positive results may lead to unnecessary biopsies (removal of breast tissue for further study) and increased anxiety for many women. At the same time, breast MRI cannot visualize the calcium deposits, known as calcifications or microcalcifications, which typically surround DCIS lesions (the suspicious area). Mammography, on the other hand, can detect these calcium deposits accurately. Finally, breast MRI is more expensive than mammography.

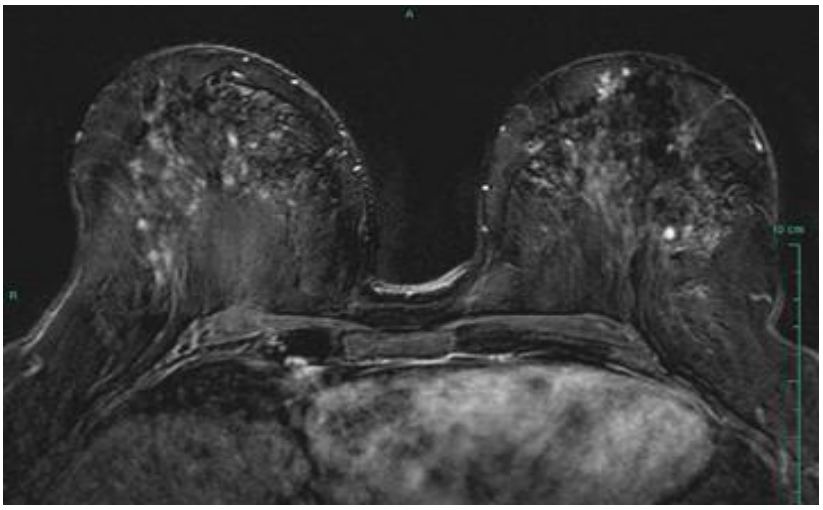

Figure 1-3 A Breast MRI with False Positive Nodule (Image courtesy: Radiological Society of North America)

1.2.3 Ultrasound Imaging

Ultrasound imaging also known as ultrasonography or simply sonography, uses high-frequency sound waves to view the internal regions of the body. It is the most economical and widely available medical imaging modality. Because ultrasound images are captured in real-time, they can also show the movements of the body's internal organs as well as the blood's passage through the blood vessels. Unlike X-ray imaging, no ionizing radiation exposure is associated with ultrasound imaging. Nowadays it is extensively used in fetal imaging, carding imaging, breast cancer detection, and detection of benign and malignant tissue in the human body.

1.2.3.1 Basic Principle of B-Mode Ultrasound

Modern medical US is performed primarily using a pulse-echo approach with a brightness-mode (B-mode) display. The basic principles of B-mode imaging are much the same today as they were several decades ago. This involves transmitting small pulses of ultrasound echo from a transducer into the body. As the ultrasound waves penetrate body tissues of different acoustic impedances along the path of transmission, some are reflected back to the transducer (echo signals) and some continue to penetrate deeper. The echo signals returned from many sequential coplanar pulses are processed (generating the envelope from echo signal) and combined to generate an image. Thus, an ultrasound transducer works both as a speaker (generating sound waves) and a microphone (receiving sound waves). An overview of the image acquisition using ultrasound is presented in Figure 1-4 and Figure 1-5. The ultrasound pulse is in fact quite short, but since it traverses in a straight path, it is often referred to as an ultrasound beam. The direction of ultrasound propagation along the beam line is called the axial direction, and the direction in the image plane perpendicular to axial is called the lateral direction. Usually only a small fraction of the ultrasound pulse returns as a reflected echo after reaching a body tissue interface, while the remainder of the pulse continues along the beam line to greater tissue depths.

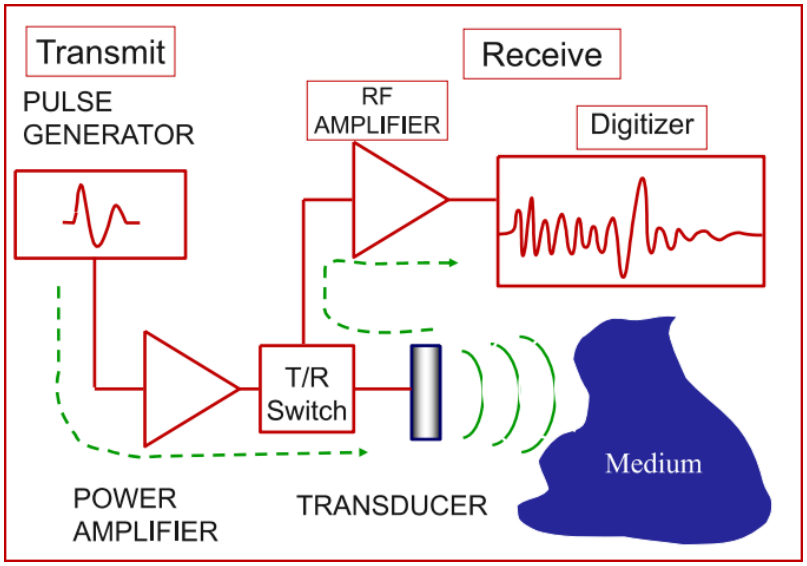

Figure 1-5 Basic Pulse-Echo Ultrasound System (Image Courtesy: Dr. S. Kaisar Alam, Rutgers University, NJ, USA)

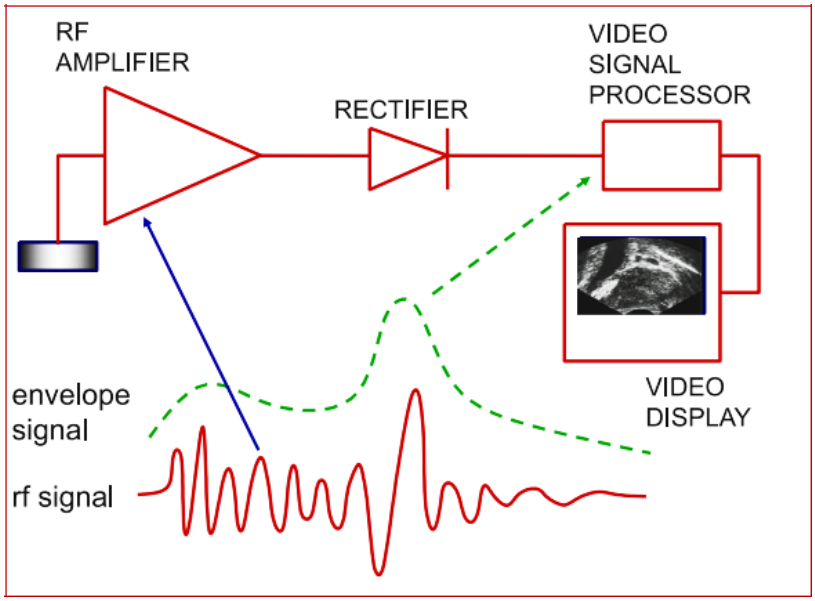

Figure 1-6 B-mode image formation (Image Courtesy: Dr. S. Kaisar Alam, Rutgers University, NJ, USA)

1.2.3.2 Challenges in Ultrasound Image Interpretation

Image artifacts are commonly encountered in clinical ultrasonography (US) and may be a source of confusion for the interpreting physician and for computer based systems. Some artifacts

may be avoidable and arise secondary to improper scanning technique. Other artifacts are generated by the physical limitations of the modality. US artifacts can be understood with a basic appreciation of the physical properties of the ultrasound beam, the propagation of sound in matter, and the assumptions of image processing. US artifacts arise secondary to errors inherent to the ultrasound beam characteristics, the presence of multiple echo paths, velocity errors, and attenuation errors. The beam width, side lobe, reverberation, comet tail, ring-down, mirror image, speed displacement, refraction, attenuation, shadowing, and increased through transmission artifacts are encountered routinely in clinical practice. Recognition of these artifacts is important because they may be clues to tissue composition and aid in diagnosis. The ability to recognize and remedy potentially correctable US artifacts is important for image quality improvement and optimal patient care.

1.2.3.3 Ultrasound imaging in Breast Cancer Detection

To address the issues of mammography and breast MRI, ultrasound imaging is considered to be one of the most effective tools as an adjunct to it [7]. Statistics show that more than one out of every four study on breast cancer detection is based on ultrasound images, and the proportion is rapidly increasing [8, 9]. Studies have demonstrated that using US images can discriminate benign and malignant masses with a high accuracy [10]. Use of ultrasound can increase over all cancer detection by 17% [11] and reduce the number of unnecessary biopsies by 40% which can save as much as $1 billion per year in the United States alone.

Breast ultrasound (BUS) imaging is superior to mammography in the following ways. (1) Since it requires no radiation, ultrasound examination is more convenient and safer than mammography

for patients and radiologists in daily clinical practice [12]. It is also cheaper and faster than mammography. Thus, ultrasound is especially suitable for the low-resource countries indifferent continents. (2) Ultrasound techniques are more sensitive than mammography for detecting abnormalities in dense breasts; hence, it is more valuable for women younger than 35 years of age [11]. (3) There is a high rate of false positives in mammography which causes a lot of unnecessary biopsies. In contrast, the accuracy rate of BUS imaging in the diagnosis of simple cysts is much higher [10]. Thus, US imaging has become one of the most important diagnostic tools for breast cancer detection.

1.3 Thesis Objectives

The context of this thesis work is a complete A Complete Semiautomated Breast Cancer Detection Approach via Quantitative and Qualitative Analysis of Breast Ultrasound (BUS) Images

This includes qualitative analysis by strain estimation method, then accurate breast lesion segmentation in US images and lastly quantitative analysis of those images. Therefore, the objective of this thesis work was to develop more robust, accurate and automatic breast lesion depiction, segmentation, quantitative analysis and then diagnosis method for ultrasound images.

The outcome of this thesis will facilitate the complete diagnosis of breast cancer.

1.4 Thesis Organization

The thesis is organized in the following way –

Chapter 2 (Background) presents the literature review and state-of-art situation of problem.

Chapter 3 Strain Estimation from Breast Ultrasound (BUS) data.

Chapter 4 Breast Lesion Segmentation

Chapter 5 Quantitative Ultrasound

Chapter 6 (Conclusion and Future Directions for Research) summarizes the whole thesis work and presents the future scope of research in BUS image segmentation problem.

2.Literature Review

2.1 Related Work

Several articles are found to address the problem of strain estimation using Breast Ultrasound (BUS) Images. Over the past several years, methods based on tissue elasticity have gained significance for diagnosis of disease [12]–[18]. These methods fall into two main groups: methods where a low frequency vibration is applied to the tissue and the resulting behavior is inspected [18]–[21], [24], and methods where a compression is 10 applied to the tissue and the resulting strain is estimated [22], [23]. Among the first group of techniques, in sonoelasticity imaging [19], [20], the vibration amplitude pattern of the shear waves in the tissue under investigation is detected and a corresponding color image (similar to color Doppler display) is superimposed on the conventional grayscale image. A theory of sonoelasticity imaging was developed [25] and in vitro results on excised human prostate were promising [26]. Among the techniques based on the estimation of tissue strain, elastography [22] is based on estimating the tissue strain using a correlation algorithm, whereas another elasticity imaging technique is based on estimating such strain using the phase information [23]. In elastography, the local tissue displacements are estimated from the time delays between gated pre- and post-compression echo signals, whose axial gradient is then computed to estimate the local strain. For QAS many sources were used for Classification of Ultrasonic B-Mode Images of Breast Masses[..]. Review of Envelope Statistics Models for Quantitative Ultrasound Imaging and Tissue Characterization and review of Quantitative Ultrasound: Envelope Statistics and Backscatter Coefficient Imaging and Contributions to Diagnostic Ultrasound for mathematical model of the distributions[,,][,,] .

2.2 Overview of the proposed method

Overview of the proposed method can be broken into three steps.

Firstly, strain estimation and finding out the lesion, then segmentation and lastly qualitative analysis.

The flow chart of the proposed method is presented in Figure 2-1.

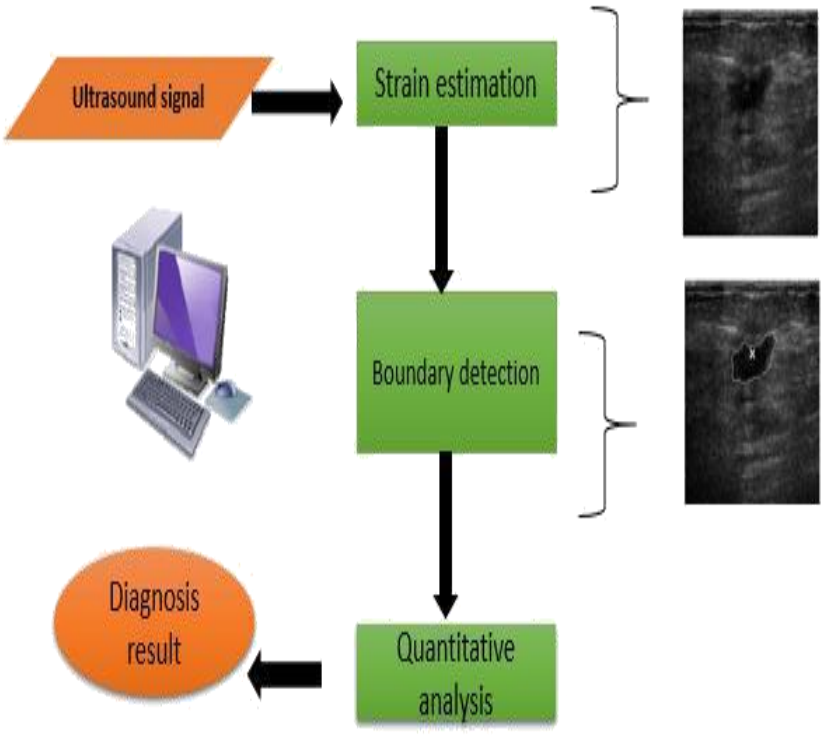

Figure 2-1 Overview of the proposed method

3. Strain Estimation

3.1 Definition

Elastography is a medical imaging modality that maps the elastic properties and stiffness of soft tissue. [28]. The main idea is to examine the stiffness of tissue for obtaining diagnostic information. Tumors, for example, scirrhous carcinoma of the breast are harder than the background tissue. [28][29]

3.2 Earlier approaches and work

The quasi-static method [28] has been applied to a broad range of clinical problems like detecting and characterizing atherosclerotic plaques, guiding minimally invasive therapeutic techniques, differential diagnosis of breast and prostate cancer, etc. [31]-[39] In this method, clinicians typically assume stress uniformity when they interpret strain elastograms as modulus elastograms. However, this assumption may produce artifacts [29]. Regrettably, no method can currently measure the internal stress distribution in vivo. Therefore, many of the 2D algorithms developed for elasticity imaging assume continuity of the displacement field due to tissue continuity [34] which may not be valid with the exception of few cases [36]. In this regard, for motion estimation, multilevel approach had been adopted earlier [39].

3.3 Objective

In that approach, the coarse displacement estimates are obtained starting from down-sampled B-mode pre and post-compression image pairs using a pyramidal processing, where in the initial level the cross-correlation threshold is 0.3. This is poor guidance displacement estimates in the succeeding levels. Although this may be claimed to be computationally efficient, this actually worsens the final displacement in case of breast lesion studies. Errors in displacement estimates in

the initial stages propagate if they are large enough that the defined search regions do not enclose the true displacements. When tissue is compressed, large and irregular local deformation can occur, which may cause local decorrelation in the recorded RF (Radio Frequency) frame pair. [34]

Moreover, for the in vivo cases, the final image might have supremacy of noise outside the lesion part which makes it harder for Clinicians to interpret and diagnose. To overcome the drawbacks of human perception-based diagnosis, researchers have been working on developing Computer-Aided Diagnosis (CAD) system. Getting rid of the complicated background not only speeds up the process, but also makes segmentation results more accurate. [37] [39]

The utilization of preceding levels only as guide sacrifices the salient features of the displacement estimates from the initial guiding levels. As the size of the kernels and search windows are larger, the guiding levels generally have less noise outside the lesion part sacrificing the clarity and sharpness of the boundary. So, the initial and final level images have contradictory features. The optimization of these facets leads to a better final strain image.

In this paper we propose a revamped multistage algorithm that solves the above issue combining images of different stages through unwarping and feature based image registration. This not only improves the prominence of lesion in the strain image but also improves the resolution whilst lowering background noises leading to quick detection of lesions, which is convenient for Computer Aided segmentation procedures.

3.4 Methodology

The method is divided into the following steps: (1) Transformation to envelope form, (2) Motion estimation using Normalized Cross Correlation NCC, (3) Displacement error correction,

(4) Repositioned fine tracking, (5) Median filtering and strain estimation in all stages, (6) Unwarping Median filtering and strain estimation in all stages, (7) Feature based image registration and final strain image

3.4.1 Transformation to envelope form

The initial step involves transforming the RF data form of the pre and post compression echo signal to the envelope or B-mode data. The B mode image contains only the amplitude information along the axial direction. Therefore, the algorithm is time optimized for computing initial stage crude displacements using B-mode images.

3.4.2 Motion Estimation Using Normalized Cross Correlation (NCC)

A kernel (matching block) is selected to estimate the displacements due to the tissue deformation independently. The kernel is then matched with the bigger search window to find the maximum similarity using normalized cross correlation method.

The corresponding displacement to this maximum similarity gives the crude peak displacements. Considering these crude displacements have a small random time shift due to physical reasons or inaccuracies in the measurement equipment, we in-corporate subsampled displacement estimation. This estimates the peak of the sampled crude displacements using 2-D parabolic interpolation. Thus sliding the kernels and search widows at a certain degree of overlap with pre-defined axial and lateral shifts, the initial displacement matrices are obtained. These matrices account both the axial and lateral displacements of the initial stage obtained from the B-mode image . This is depicted in figure number 1.

3.4.3 Displacement Error Correction:

After motion or displacement tracking at each stage, we utilize the normalized cross-correlation coefficient as a confidence measure corresponding to the reliability of the displacement estimate. Displacement estimates with a low normalized cross-correlation coefficient (less than 0.8) are discarded and then interpolated from surrounding displacement estimates that possess a higher normalized cross-correlation value.

3.4.4 Repositioned Fine Tracking:

Next the size of kernel and the search window is diminished to find out the finer displacements using the earlier stated method. This reduces decorrelation noise. However, in this case the block matching is initiated after the search window is repositioned utilizing the initial stage displacements, to ensure the confinement of the tracked tissue within the search window with a restricted range to minimize false peak error as far as possible. This procedure is implemented according to the steps below:

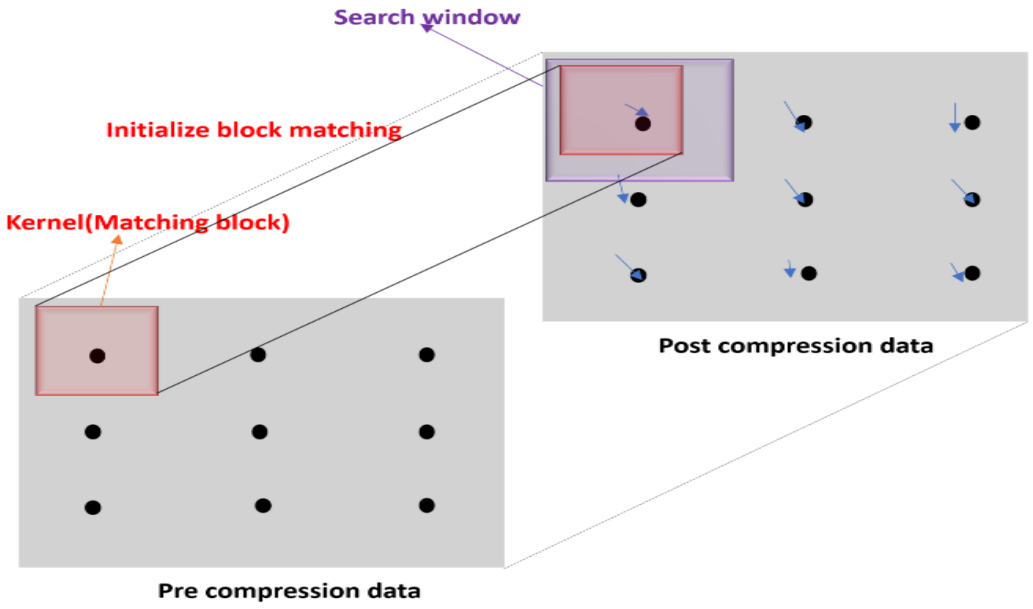
Search window
Initialize block matching
Kernel(Matching block)
Post compression data
Pre compression data

1-a

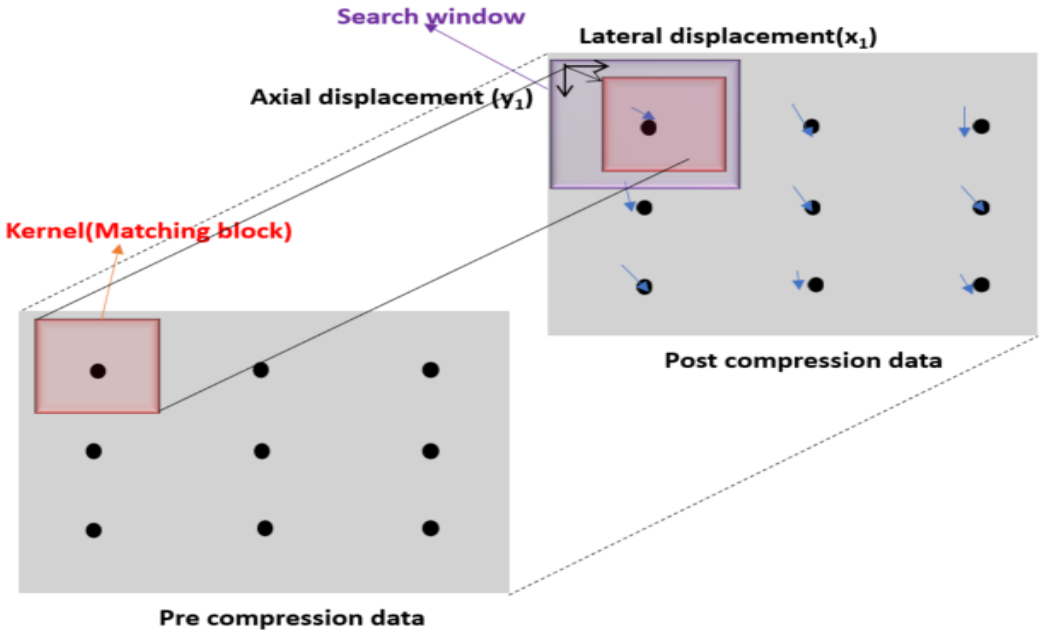
Search window
Lateral displacement(x_1)
Axial displacement (y_1)
Kernel(Matching block)
Post compression data
Pre compression data

1-b

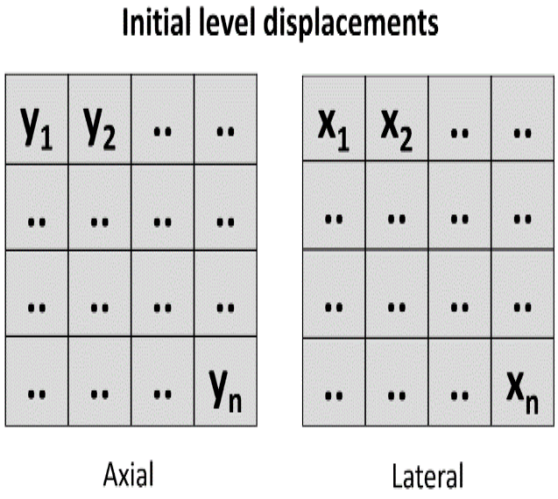

1-c

Figure 3-1 .Initial motion estimation: (a) Defining kernel, search window and shifts size (b) Initial motion tracked using NCC (c) Initial stage displacements

a. Initial stage displacements are mapped into a grid that replicates the dimensions of the next stage displacement matrices (larger) utilizing cubic-spline interpolation. which we term as" reference displacements".

b. Search window is repositioned using the reference displacement matrices and then step B is iterated again with smaller kernel, search window and smaller window shifts. This is demonstrated using figure 2.

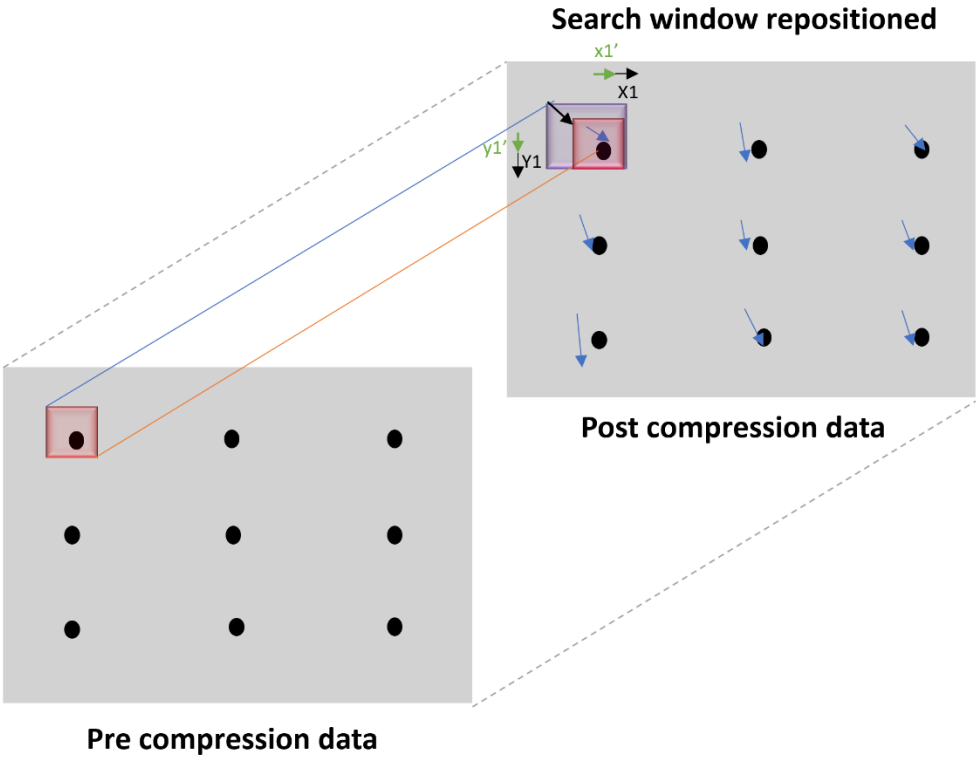

Figure 3.2: Repositioned motion tracking. x1' and y1' (in green) indicate reference displacements X1 and Y1 indicates fine tracked displacements. Total displacement after this stage is vector addition of these two i.e. x1'+X1 and y1'+Y1

At the end of n stages, the motion vector is given as $L=L_1+L_2+L_3+L_4+\ldots\ldots L_n$ (1)

where $L_1, L_2, ..L_{n-1}$ are cumulatively mapped into stage n grid

For a 4 stage implementation, the final motion vector is the vector summation of the displacments obtained at each stage depicted in figure 3.

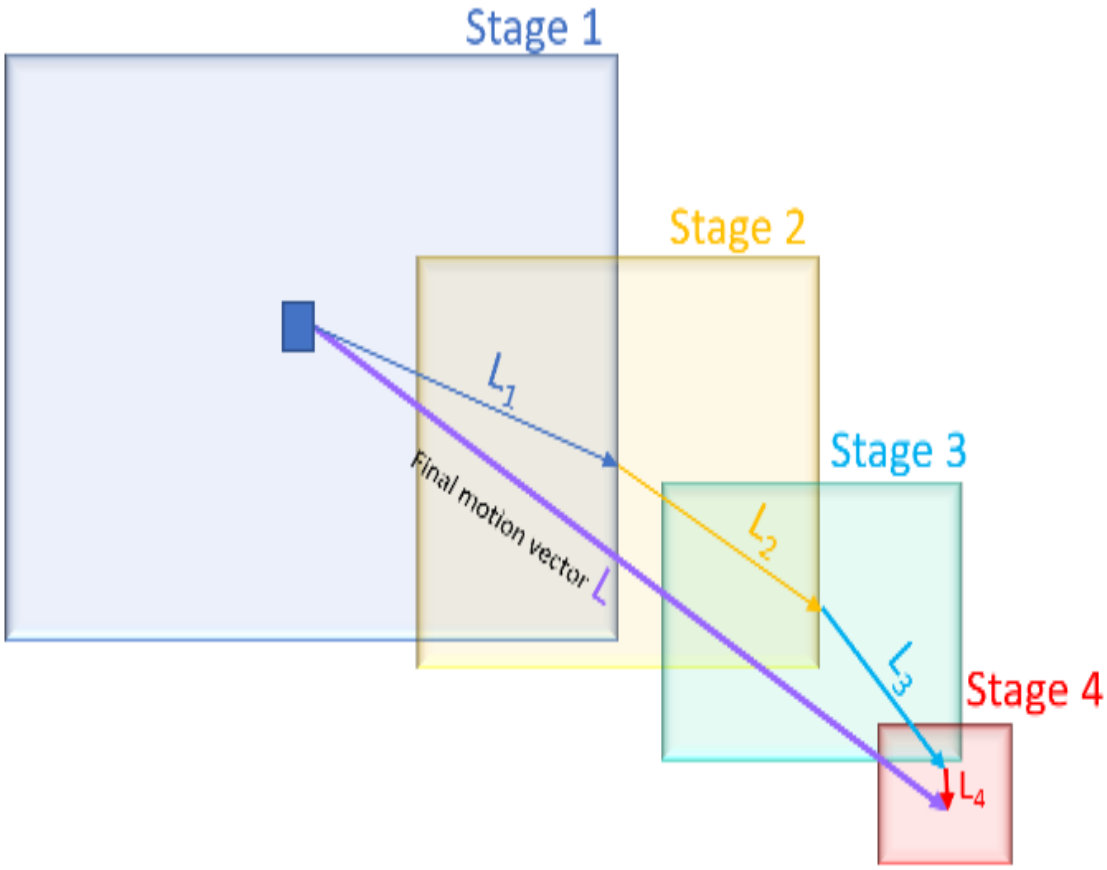

Figure 3.3. Final motion vector at the end of 4stages

3.4.5Unwarping:

A method to compensate the deformation at pixel level through using the motion estimates from the earlier levels is the main idea of unwarping. After obtaining the displacements from the multistage algorithm, we use the displacements to unwarp the post compression RF signal at each pixel through transforming multistage grid to the post data grid and interpolating the intermediate values through spline interpolation to form lag compensated unwarped post (LCUP) data. Again, block matching procedure of step B is incorporated to find out the displacements between pre and lag compensated unwarped post (LCUP). The vector summation of the displacement matrix

of this unwarping procedure and the multistage procedure in a grid equivalent to dimensions of the unwarping procedure give the true final stage displacements. Therefore, it accounts for the residual motion that multistage algorithm does not take into account.

3.4.6 Median Filtering and Strain Estimation in All Stages:

Displacement matrix is median filtered to reduce the effect of the shot noise at the cost of some spatial resolution. The median filtering parameter is applied according to the resolution of the displacement estimates corresponding to the stages. 3X3, 5x5, 7x7 were used empirically in the method. In the presence of large, irregular and non-axial tissue motions in case of patient data, major echo-signal decorrelations occur and cause conventional gradient based strain estimators to fail. To overcome this, we have used the least square estimation to compute the strain matrices corresponding to the displacements at each stage

3.4.7 Feature Based Image Registration And Final Strain Image:

Feature-based image registration establishes a correspondence between a number of points in images, a geometrical transformation is then determined to map the target image to the reference images, thereby establishing point-by-point correspondence between the reference and target images [39]. The strain images of all the stages are mapped in a pre-compression data equivalent grid through the aforementioned feature-based image registration to take account of prominent features of each corresponding stage. Then a suitable weighted average of the registered images produces the final strain image.

3.5 Strain Estimation Results

We have incorporated our algorithm and proposed method on sets of patient data i.e. *in vivo* breast data. The *in vivo* breast data for this paper are chosen from an existing dataset of 33 cases of age 20 to 75 years. These data include both cancers and fibroadenomas and were acquired with free hand compression. A sP500 (Ultrasonix Medical corporation, Richmond, Bc, Canada) scanner with a l14–5/38 probe was used by Dr. Brian Garra at the University of Vermont to acquire the data. The probe operated at 10 MHz (nominal). The study was approved by institutional review board and consent was obtained from each of the patient.

We implemented a 4-stage computation along with the unwarped stage on several data sets. The processing parameters for the dataset of 2100*128 after the initial step A of the algorithm are summarized in the table below:

	1st stage	2nd stage	3rd stage	4th stage	Unwarped
KERNEL	128 *12	64*8	32*6	32*6	32*6
SEARCH WINDOW	192 * 16	86*12	44*8	44*8	44*8
Shift	64*2	32*2	16*2	10*1	10*1

Here A*B refers to A being axial pixels utilized and B being lateral pixel utilized.

These parameters are independently set and after computation of axial strain images of different stages, these are registered in a grid equivalent to the pre-compression data size grid with a weightage of [0.1 0.1 0.1 0.1 0.2 0.5] to produce the final strain image.

From the SNR plot, it is evident that the proposed method has more SNR compared to the other methods like 1D strain estimation and the unwarped stage. Thus, this not only improves the resolution by a factor of 60 from typical block matching but also has a higher SNR whilst preserving the clarity of boundaries. Thus, this not only improves the process with respect to quantitative analysis it also helps immensely in quantitative analysis work fields due to higher SNR and less complicated backgrounds. The clear depiction of the boundaries of the tumor aids in calculating and analyzing the roughness factor for quantitative analysis.

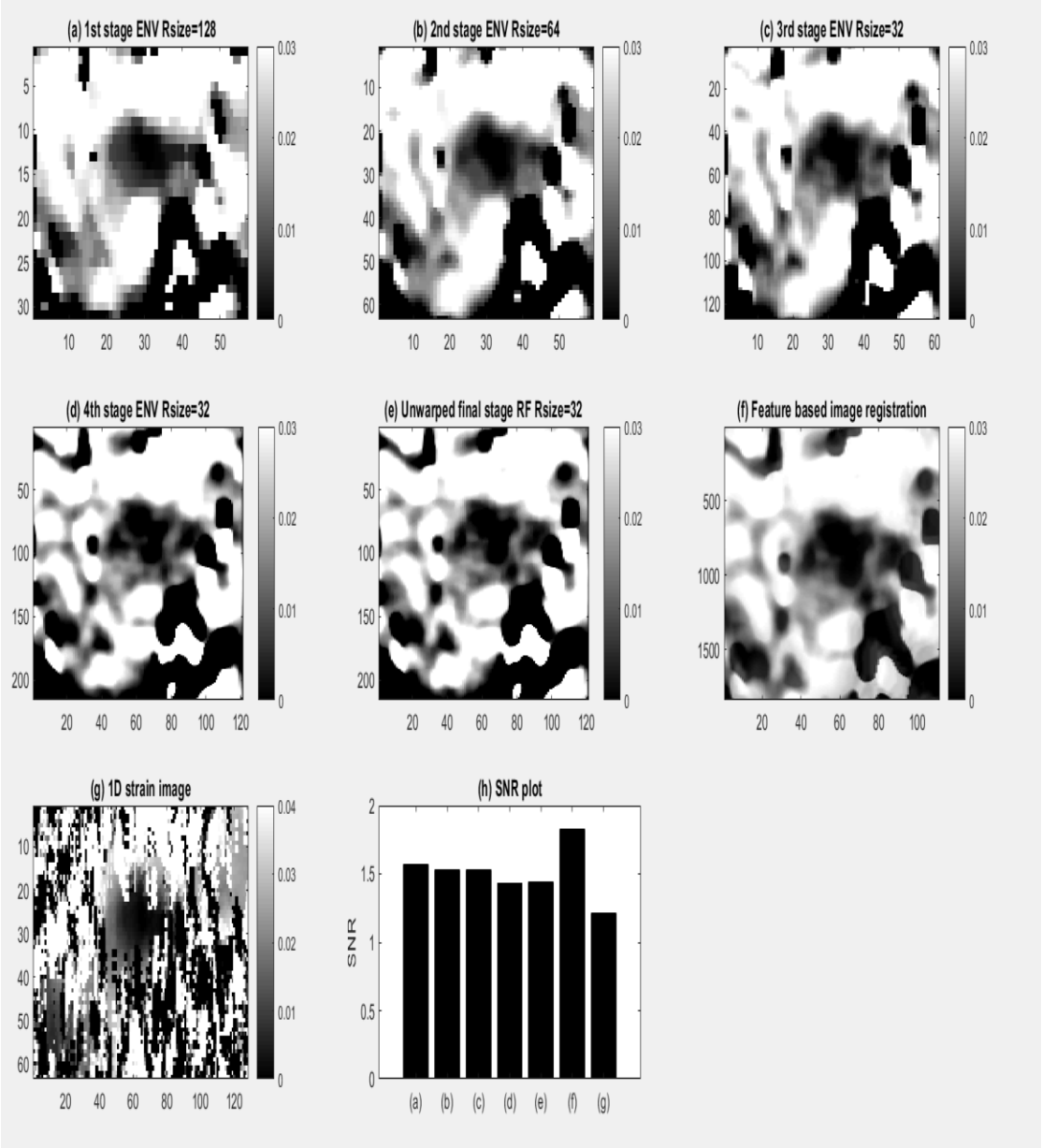

Figure 3-5: axial strain image for (a) Basic 2d block matching i.e. 1st stage Envelope (b) 2nd stage Envelope (c) 3rd stage Envelope (d) 4th stage Envelope (e) Unwarped final stage RF (f) Proposed featured based multistage strain estimation (g) 1D axial strain image (h) Comparative SNR plot.

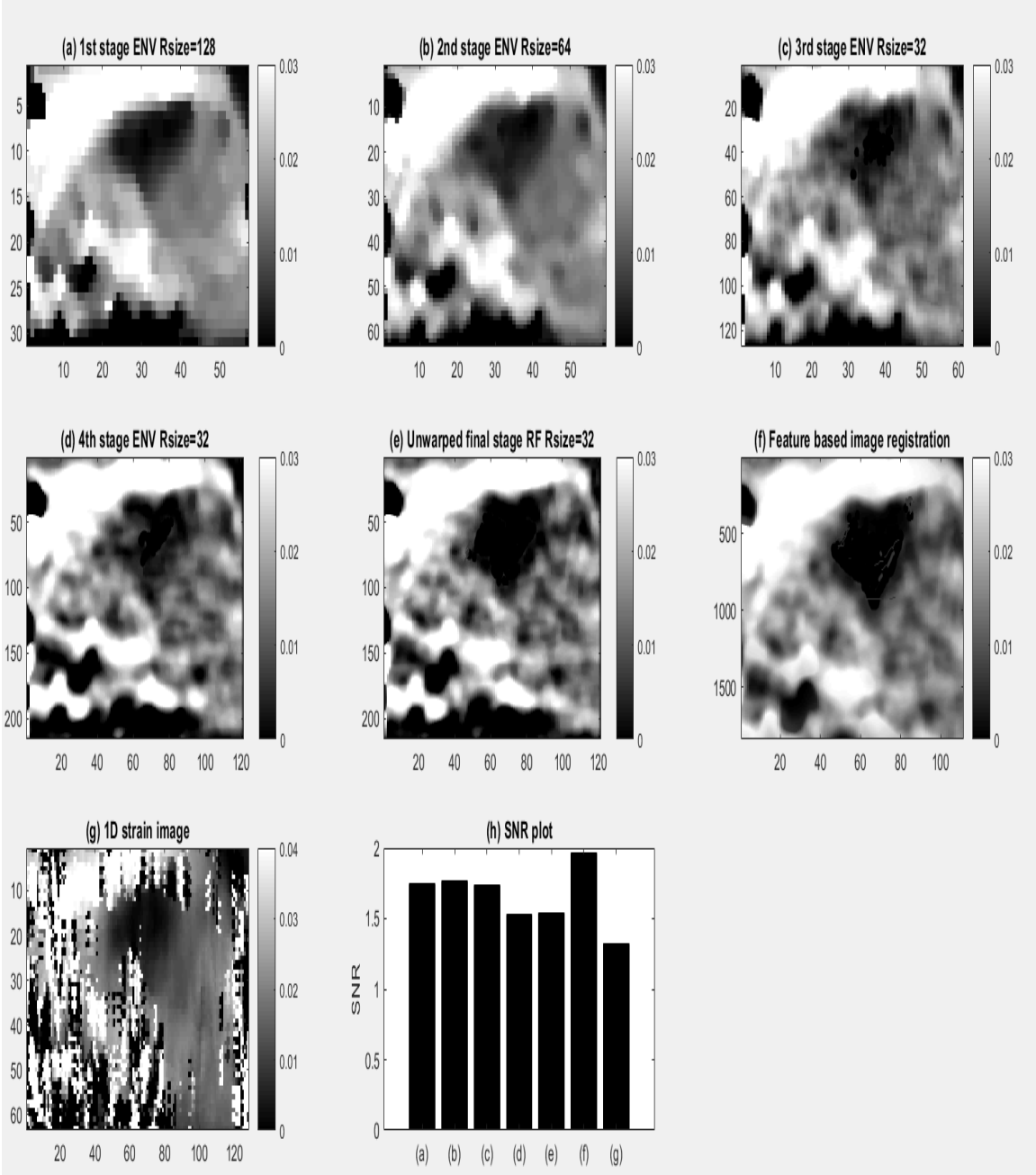

Figure 3.6 Axial strain image for (a) Basic 2d block matching i.e. 1st stage Envelope (b) 2nd stage Envelope (c) 3rd stage Envelope (d) 4th stage Envelope (e) Unwarped final stage RF (f) Proposed featured based multistage strain estimation (g) 1D axial strain image (h) Comparative SNR plot.

4 Breast Lesion Segmentation

Segmentation of BUS images still remains challenging mainly due to the inherent artifacts of ultrasound images such as speckle noise, low signal/noise ratio, blurry edges and poor quality [16]. The existing algorithms address the segmentation problem by processing the information available from a single frame of image whereas the human observers have access to more information than just one frame of image. They observe the same lesion from multiple views by sweeping through number of planes which is not the case when we process one image to delineate boundary using computer. Moreover, the quality of the acquired images are dependent on the skills of the operator and parameter settings of the machine. These factors make lesion detection and delineation a very difficult task for the computer. One of the main objectives of this thesis was to design an efficient and automatic lesion segmentation algorithm for breast ultrasound images.

In this chapter, we describe the image map improvement techniques and final segmentation framework proposed for segmentation of breast lesion.

4.1 Introduction

Acousto-elasticity in biological soft tissues has been adapted to relate the mechanical properties of tissue and its loading to the load-dependant changes in acoustic behavior [1, 2, 3]. For example, ultrasound images can be used to diagnose tendinopathy by segmenting the image into regions that delineate the mechanical differences between intact and pathologic regions of tendons. Many standard techniques require manual intervention in the analysis of the image, and it is desirable to automate as much of the image processing as possible. This paper presents a new way of segmenting multiple frames of ultrasound video based only on an initial indication of the region of interest.

Most current image segmentation algorithms are designed for segmenting a certain Region of Interest (ROI) from a single frame. For example, a texture discriminant is proposed for characterizing B-scans of Achilles' tendon in [4]. A filter algorithm is proposed for equine tendon structure identification in [5]. A watershed segmentation algorithm was applied to breast tumor in [6]. The active contour (snake) model in [7],[8] is an energy-minimizing spline guided by external constraints and influenced by image that pull it toward features such as lines and edges. All of these images segmentation algorithms derive the threshold value using only features of the ROI. In contrast, the proposed Projected Empirical Segmentation (PES) algorithm locates the values by comparing features from within the ROI with features from a region known to be outside the ROI. This allows application of more advanced techniques from pattern recognition to give a more accurate segmentation.

Different image frames from the video may carry different amounts of information. For example, some frames may be blurrier than others and more difficult to segment. This paper proposes PES as a way to segment the ROI that combines two special features: projected segmentation and empirical segmentation. The algorithm divides the local region of the image into three parts: the internal region, an intermediate region, and the external region. By comparing the differences in the feature vectors between the internal region and the external region, the algorithm acquires empirical values that allow separation of the intermediate region. Once the current frame is segmented, the algorithm projects onto the next frame, including the initial ROI and the empirical values to prevent the performance of the algorithm being compromised due to the variation in the image quality.

4.2 Image Pre-processing for Segmentation

The main aim for image pre-processing is to increase homogeneity inside the tumor lesion and enhance the tumor boundary by using standard image processing techniques. The proposed image pre-processing scheme for our segmentation framework is illustrated in Figure and discussed in details in next subsequent subsections.

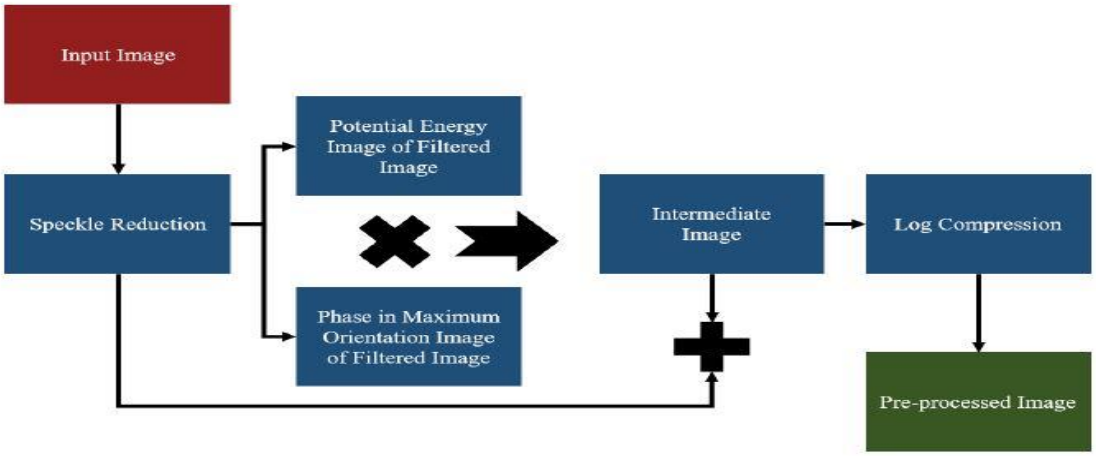

4.3 Speckle Reduction

Speckle is a particular kind of noise which affects ultrasound images, and can significantly reduce their quality and diagnostic usefulness [17]. The main aim of ultrasound de-noising methods is both to produce of image of standard appearance with reduced level of speckle for improving the appearance of images but importantly for image analysis, both intensity inhomogeneity and speckle can challenge intensity-based segmentation methods [18]. The speckle reduction algorithm should focus reducing speckle while preserving anatomic information is

necessary to delineate reliably and accurately the regions of interest and to carry on important diagnostic image analysis [19]. In our framework, we have used a recent approach for speckle reduction proposed in [19]. In [19], authors proposed an adaptation of the Non Local means (NL-means) method to a dedicated US noise model [20] using a Bayesian motivation for the NL-means filter [21]. Figure presents the result of speckle reduction step. It is to be noted that the major anatomical details are preserved in the filtered image with a reduced level of speckle noise. The output image of the filter has less granular appearance than the original image but structure of lesion of the lesion is well preserved with increased homogeneity inside the lesion

4.4 METHOD

4.4.1 PES (Projected Empirical Segmentation)

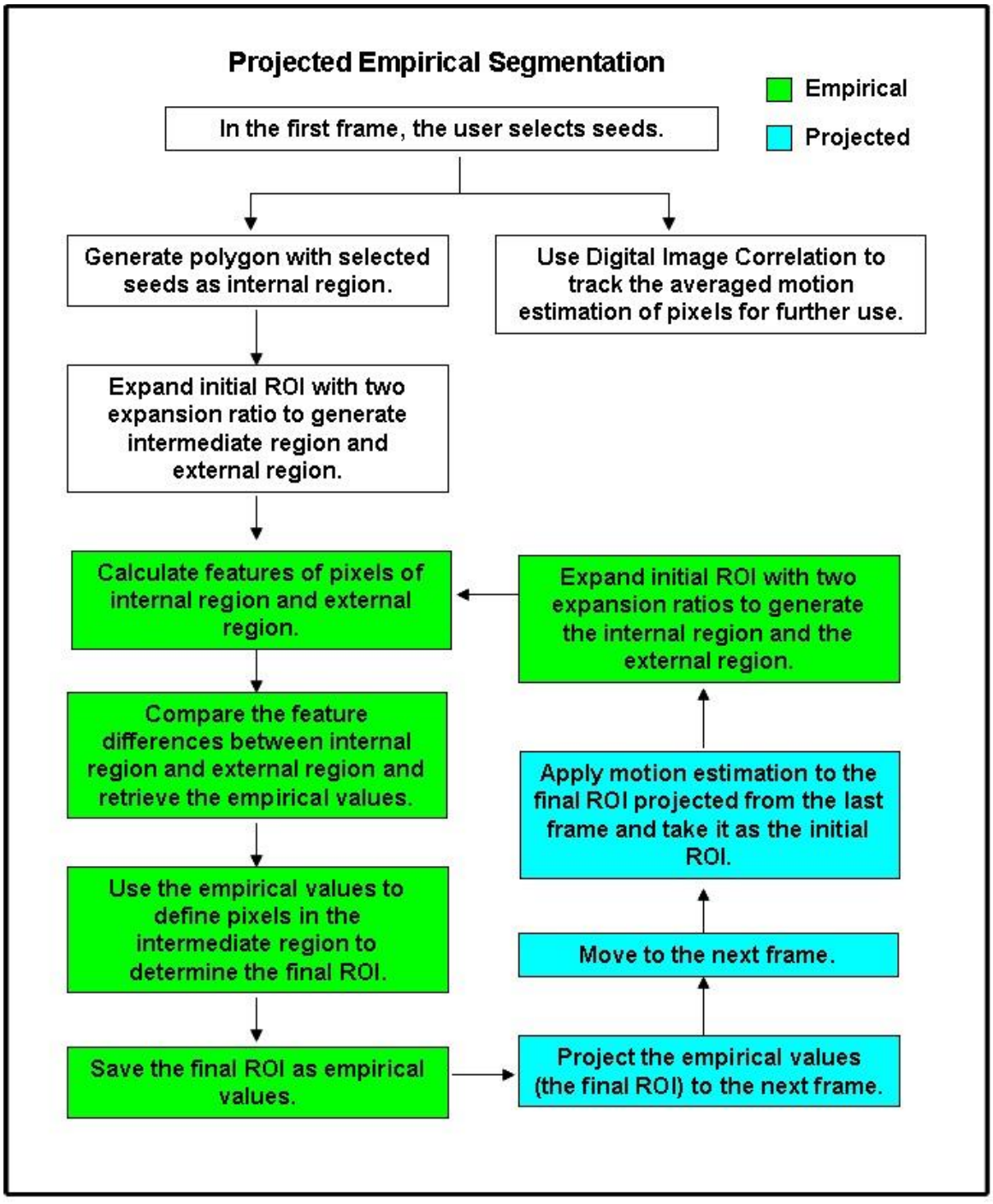

Figure 1: Flow chart of procedures of Projected Empirical Segmentation.

The empirical segmentation generates three regions: the internal region, the intermediate region, and the external region. The internal region is assumed to be inside the final ROI, the external region is assumed to be outside the final ROI, and the intermediate region is a region whose pixels need to be categorized. The statistics of the features of the two known regions are calculated. The statistics of the features of each point in the intermediate region are then compared to the statistics of the two known regions using a separating hyperplane determined from a Least Squares fit. Once the intermediate region is segmented, the final ROI for this frame can be drawn. The empirical values are the boundaries of this final ROI in the intermediate region.

Projected segmentation enables the algorithm to project information from the current frame into succeeding frames. The projected information includes the boundaries of the final ROI of the current frame, where the empirical value is used as an initial estimate of the regions in the next frame. Projected segmentation helps insure that the algorithm performs well even when the image quality degrades. The projection also creates the initial region in the succeeding frame by combining the final ROI and the motion estimation. It decreases the time needed to estimate the internal region and removes the need for the user to manually intervene in succeeding frames.

The algorithm begins by requiring the user to specify a seed region in the first frame, whose polygonal convex hull is assumed to lie within the ROI. Two expansion ratios are applied to create two new regions: the external and the intermediate. The external region is assumed to lie outside the final ROI, and the intermediate region is a region whose pixel needs to be examined. Once the three regions are generated, the algorithm calculates the statistics of features of points in both the internal and external regions. By comparing the differences in the statistical features of the two regions, an empirical value is calculated through minimum squared-error and pseudo inverse equation, as used for pattern classification in Duda, Hart, and Stork [12]. The algorithm then

calculates the statistical features of points in intermediate region and compares with the empirical value, so the decision can be made and the final ROI determined. The algorithm then retrieves the boundaries of the final ROI and saves the information for projection into the next frame.

Starting with the second frame, the algorithm requires no manual intervention from the user. In all succeeding frames, the initial region is created by combining motion estimation and final ROI from the previous frame. The motion estimation evaluates the shift of points along frames, and the final ROI from previous frame defines the shape of the ROI. Together, these determine the shape and the location of the initial region in the next frame. The internal region is created by contracting the initial region by 0.8. Again, two expansion ratios are applied to create the intermediate and external regions. By comparing the statistical features of the two regions, the empirical value is retrieved and used to examine the statistical features of every point in the intermediate region to determine the final ROI of current frame. Once the final ROI is determined, the algorithm recalculates the boundaries of the final ROI and saves them as information to project to the succeeding frame. The algorithm repeats through all the remaining frames.

4.4.2 Expansion Ratio

The expansion ratio creates a new region by enlarging the internal region. Suppose (x, y) is a boundary pixel of internal region, ($\bar{x}$, $\bar{y}$) is the center of interior region, and (x', y') is the boundary pixel of the enlarged region with the same normalized vector to ($\bar{x}$, $\bar{y}$) as point (x, y). The location of (x', y') and the expansion ratio can be determined by the following equations:

$$\frac{\left(x'-\bar{x}, y'-\bar{y}\right)}{\sqrt{\left(x'-\bar{x}\right)^2+\left(y'-\bar{y}\right)^2}} = \frac{\left(x-\bar{x}, y-\bar{y}\right)}{\sqrt{\left(x-\bar{x}\right)^2+\left(y-\bar{y}\right)^2}} \quad (1)$$

$$\text{Expansion Ratio} = \frac{\sqrt{\left(x'-\bar{x}\right)^2+\left(y'-\bar{y}\right)^2}}{\sqrt{\left(x-\bar{x}\right)^2+\left(y-\bar{y}\right)^2}} \quad (2)$$

Let P_{INT} be the data set of the location of points in the internal region. Applying an expansion ratio IR creates a larger region P_A that encloses the internal region (P_{INT}). The intermediate region P_{MID} is given by:

$$P_A = IR \times P_{INT} \quad (3)$$

$$P_{MID} = \left[(x,y) \in P_A\right] \cap \left[(x,y) \notin P_{INT}\right] \quad (4)$$

The second expansion ratio ER is applied to create another region P_B that encloses both the internal region and the intermediate region. The external region P_{EXT} is given by:

$$P_B = ER \times P_{INT} \quad (5)$$

$$P_{EXT} = \left[(x,y) \in P_B\right] \cap \left[(x,y) \notin P_A\right] \quad (6)$$

The expansion ratio IR is initialized to 1.3 while the expansion ratio ER of biomedical tissue is usually between 2.5 and 3 (though it may vary with different tissue characteristics). The expansion ratio may be adjusted automatically in order to ultimately fit the data.

4.4.3 Motion Estimation

Digital image correlation is an optical registration algorithm used to isolate, track and compute features of a region of interest through frames which are slice from a time series by a digital sonograph video. It is capable of calculating the accurate measures of mechanical deformations, displacement and strain in both two and three dimensions [9] [10] [11]. The basic concept of digital image correlation is to track the location of data set in different frames by minimizing the feature difference of selected data sets in different frames.

$$Correlation = \sqrt{\Sigma_i \Sigma_j \left[A(X_i, Y_j) - B(X_i^*, Y_j^*)\right]^2} \quad (7)$$

Suppose array A, B are corresponding subsets in two digital images, and coordinates (X_i, Y_j) and (X_i^*, Y_j^*) are related by the deformation which occurs between two images. $A(X_i, Y_j)$, $B(X_i^*, Y_j^*)$ are the individual intensity of point (X_i, Y_j) and (X_i^*, Y_j^*) in each subset. Assuming small subsets from the intensity pattern stored in array B are related to small subsets of the same size in array A by a homogeneous linear mapping, the correlation is the square root of the sum of the squared intensity difference between corresponding pixels. Digital image correlation relates the corresponding pixels (X_i, Y_j) and (X_i^*, Y_j^*) by optimizing (minimizing) the correlation value.

4.5 Statistical Features

Statistical features are keys for the successful application of empirical segmentation since they are used to distinguish the final ROI from the external region. In the PES algorithm, the statistical features are a collection of moments, which are the combinations of the pixel intensity and different orders of distance. These are adapted from [13].

$$\mu_{PQ} = \sum_{y=\bar{y}-2}^{y=\bar{y}+2} \sum_{x=\bar{x}-2}^{x=\bar{x}+2} (x-\bar{x})^P (y-\bar{y})^Q f(x,y) \quad (8)$$

Suppose $\bar{x}$ and $\bar{y}$ is the location of the pixel, x and y is the location of its surrounding pixel, and f(x, y) is the intensity of point (x, y). P and Q are the number of order of the distance factor, which usually varies from 0 to 3.

$$\mu_{00} = \sum_{y=\bar{y}-2}^{y=\bar{y}+2} \sum_{x=\bar{x}-2}^{x=\bar{x}+2} (x-\bar{x})^0 (y-\bar{y})^0 f(x,y) \quad (9)$$

$$\mu_{20} = \sum_{y=\bar{y}-2}^{y=\bar{y}+2} \sum_{x=\bar{x}-2}^{x=\bar{x}+2} (x-\bar{x})^2 (y-\bar{y})^0 f(x,y) \quad (10)$$

$$\mu_{02} = \sum_{y=\bar{y}-2}^{y=\bar{y}+2} \sum_{x=\bar{x}-2}^{x=\bar{x}+2} (x-\bar{x})^0 (y-\bar{y})^2 f(x,y) \quad (11)$$

With these moments, the normalized central moments, denoted as η_{pq}, can be defined as

$$\eta_{PQ} = \frac{\mu_{PQ}}{\mu_{00}^r} \quad (12)$$

where

$$r = \frac{P+Q}{2} + 1$$

A set of invariant moments can be derived from the second and third moments:

$$\phi_1 = \eta_{20} + \eta_{02} \quad (13)$$

$$\phi_2 = (\eta_{20} - \eta_{02})^2 + 4\eta_{11}^2 \quad (14)$$

$$\phi_3 = (\eta_{30} - 3\eta_{12})^2 + (3\eta_{21} - \eta_{03})^2 \quad (15)$$

$$\phi_4 = (\eta_{30} + \eta_{12})^2 + (\eta_{21} + \eta_{03})^2 \quad (16)$$

The algorithm uses a five by five matrix centering at each pixel and calculates the seven moments (μ_{00} , μ_{20} , μ_{02} , ϕ_1 , ϕ_2 , ϕ_3 , ϕ_4). This helps prevent the influence of inconsistent speckles and other irregularities, which are often noise.

4.6 Results

Acoustoelastic Strain Gauge method [3] can successfully distinguish healthy tendon from the damaged ones. However, it is limited to analysis of a spatially fixed region of interest. In other words, it is in need of a certain region of interest as input for further mechanical analysis. Therefore, the PES algorithm combines digital image correlation and moment-based region growing to accomplish the segmentation. The algorithm has been tested on tendon ultrasound images to separate the region of tendinopathy from the rest of the tendon for mechanical analysis through Acoustoelastic Strain Gauge.

Tendinopathies can include regions of inflamed regions (tendinitis) and pathological region without inflammation (tendinosis). In both cases, the region is mechanically altered and compromised. It usually requires an experienced radiologist to diagnose the tendonitis from ultrasound images. The PES algorithm may help to segment the region of tendonitis from the remainder of the tendon in ultrasound image to enhance further quantitative or qualitative analysis.

Figure 2 is a result of segmenting tendinopathy from the rest of the tendon image. In Figure 2(a), the bright curve on the right is the surface of calcaneus. The relatively dark elliptical region on top of calcaneus (in this image) has been diagnosed as tendinopathy. Our algorithm is applied to segment the tendon from the rest of the image with expansion ratio (ER) 2.65, and the result is as Figure 2(b). PES segments the regions of tendinopathy and tracks in throughout the subsequent video images.

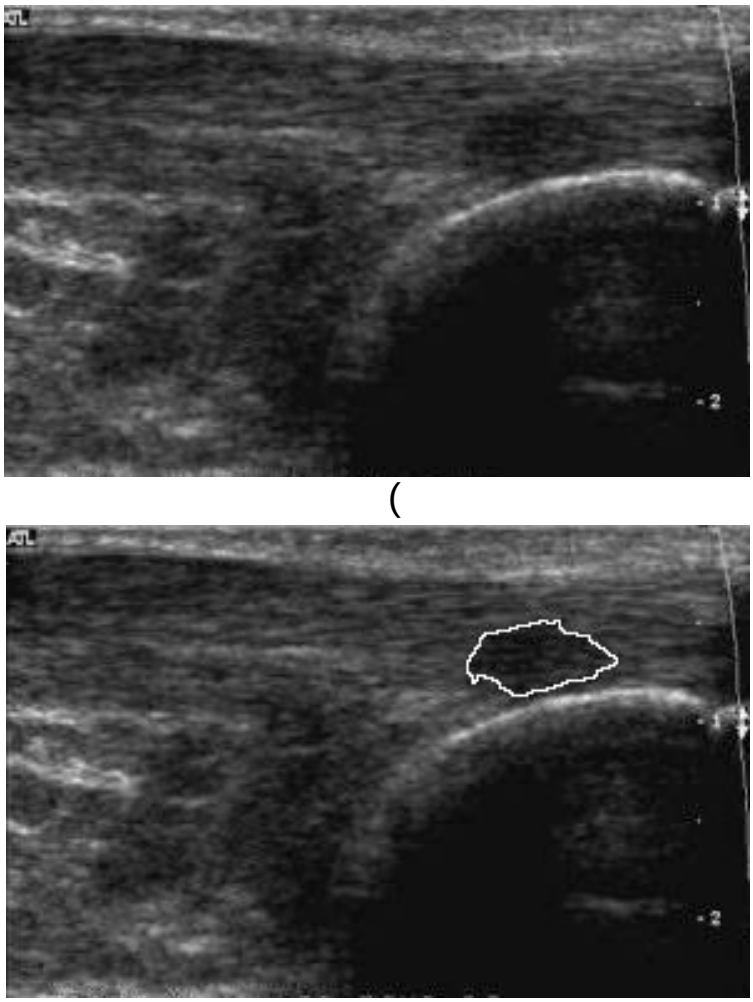

Figure 2: An ultrasound image of a human Achilles tendon (a) and the result of our segmentation to late the tendinopathy (b)

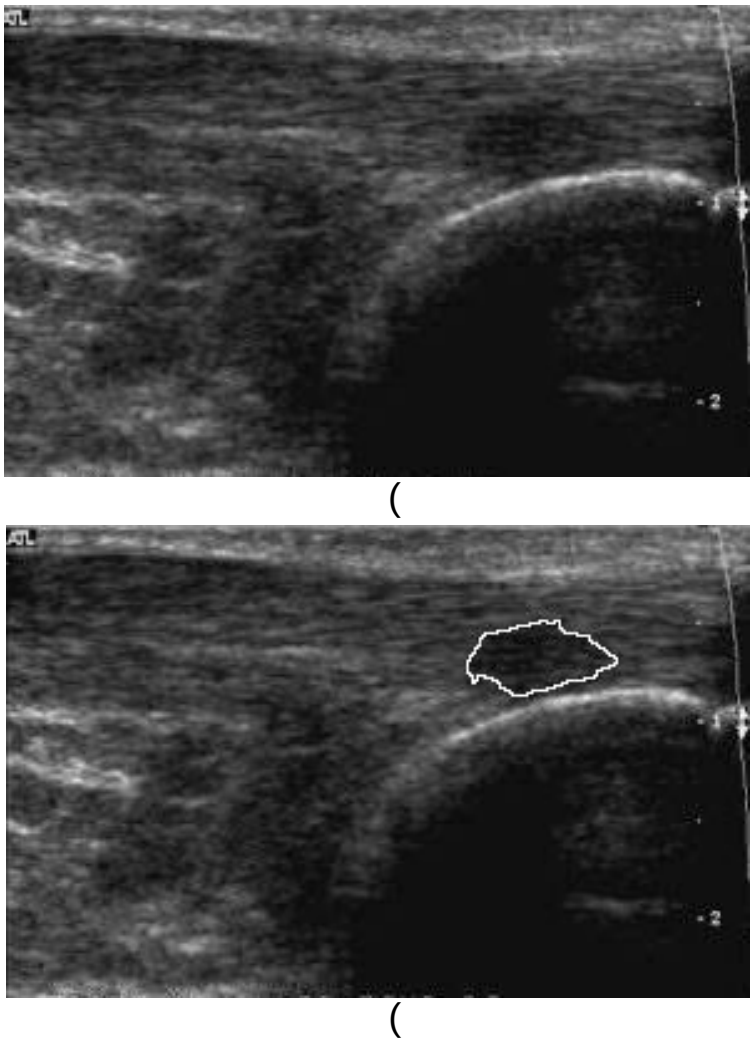

Figure 3: An ultrasound image of a human Achilles tendon (a) and the result of our segmentation to late the tendinopathy (b)

Other than tendon ultrasound images, our algorithm has also been applied to blood vessel images, and it has also shown promising results. Figure 4 shows how the algorithm can segment an abdominal aorta from the rest of the ultrasound image taken from a rat. In Figure 4(a), the dark region on upper left is caudal vena cava. The dark region at the right of caudal vena cava is superior mesenteric artery, and the dark region under superior mesenteric artery is abdominal aorta. Our algorithm is applied to segment abdominal aorta from the rest of the image with expansion ratio

(ER) 2.8, and the result is as Figure 4(b). Post hoc analysis of the images tracks the rapid changes in cross-sectional area with the beating of the rat heart (~400 BPM).

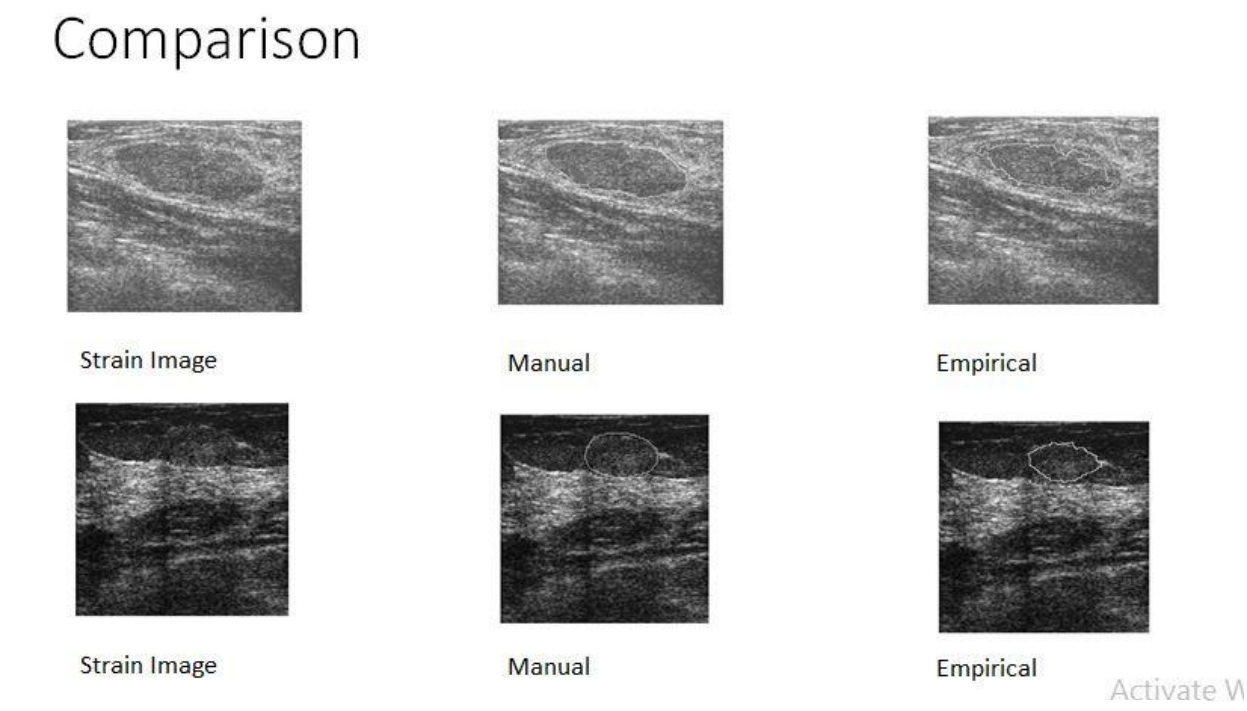

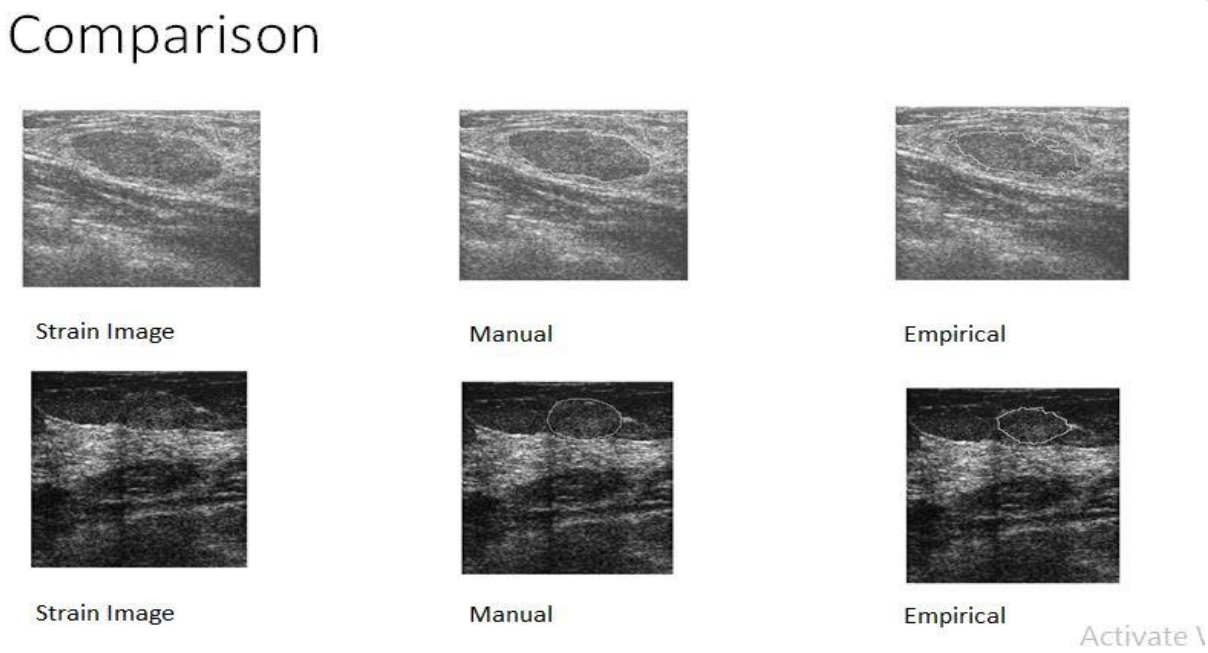

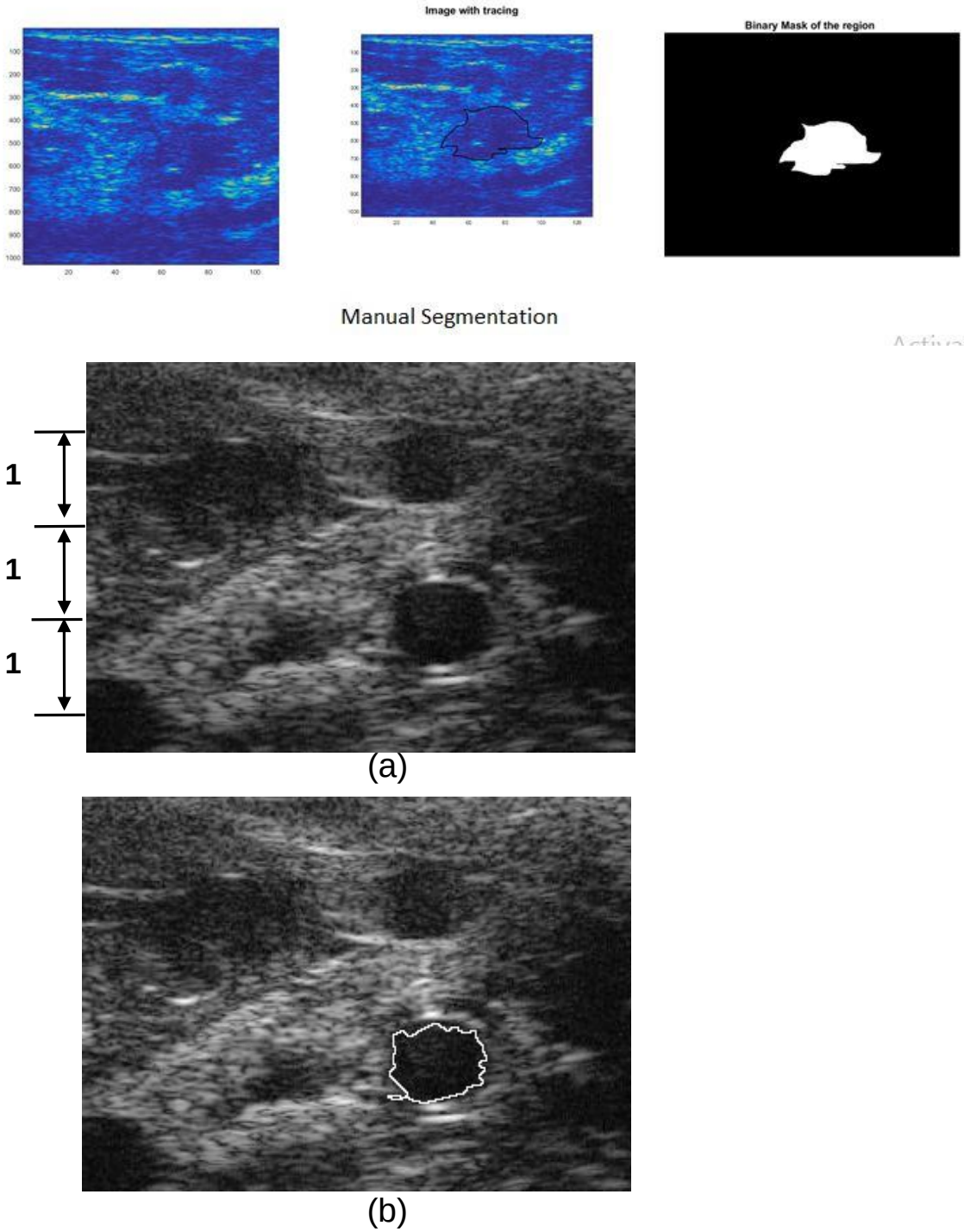

Figure 4: An ultrasound image of an abdominal rat aorta (a) and the result of our segmentation (b)

4.7 Simulation

One of the difficulties in assessing the performance of the PES method is that the true answer to a given problem is unknown. This can be addressed by creating a synthetic target where the correct answer is known a priori, and then comparing the performance of PES with another standard method (such as region growing [14][15]) and then comparing the two estimations to the correct answer. Since the ultrasound images consist of a large number of scattered points, an appropriate target may be synthesized by choosing two (independent) distributions of points, one within a target area (chosen to be an ellipse) and the other outside the target area. For these simulations, the in-area distribution is "salt-and-pepper" noise with 10% in-area and with 28% out-of area. The density of the distribution is determined by using the averaged intensity of biomedical ultrasound image, such as Figure 2, as reference. The total number of points enclosed in the ellipsoidal targets it 5641.

Figure 5(a) is a designated image for simulation. The ROI of the image locates on the upper left part of the image marked by the white ellipse boundary. Figure 5(b) is the result of ROI segmented by PES whose boundary is marked in yellow line, whereas Figure 5(c) is the result of ROI segmented by Region Growing whose boundary is marked in blue line. The simulation shows PES has better performance with higher accuracy and efficiency than region growing segmentation does.

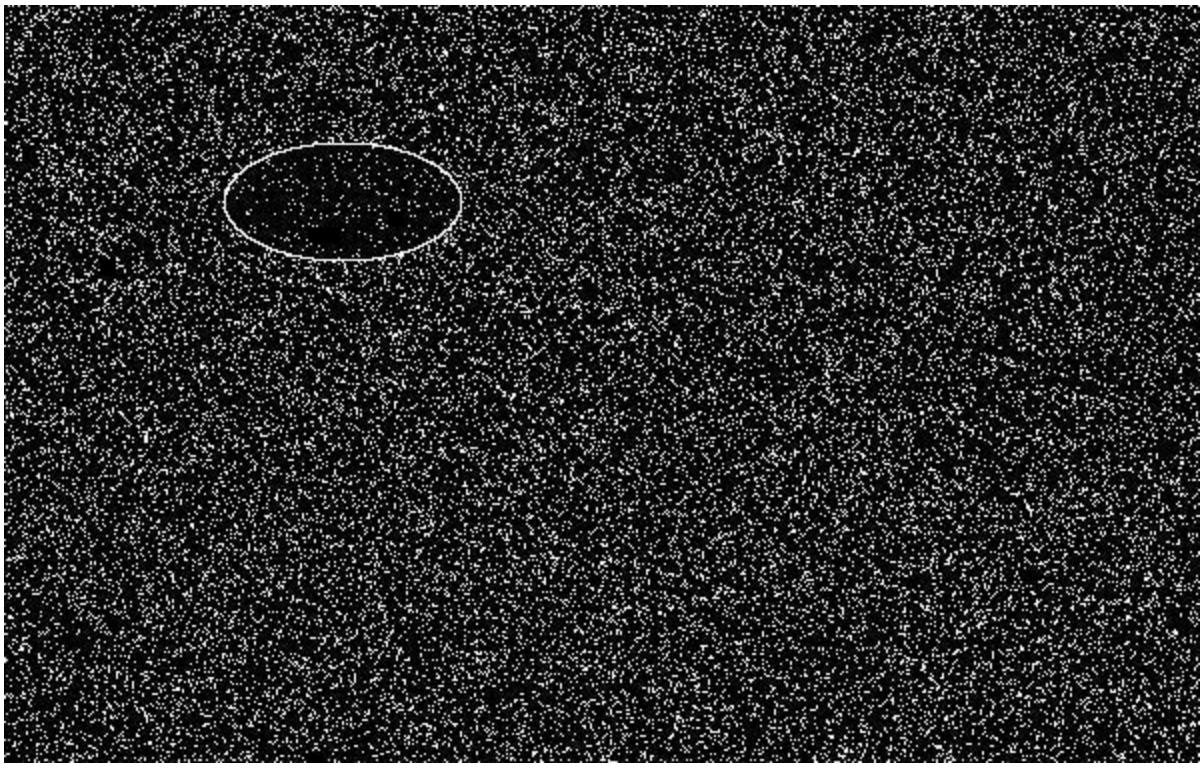

(a)

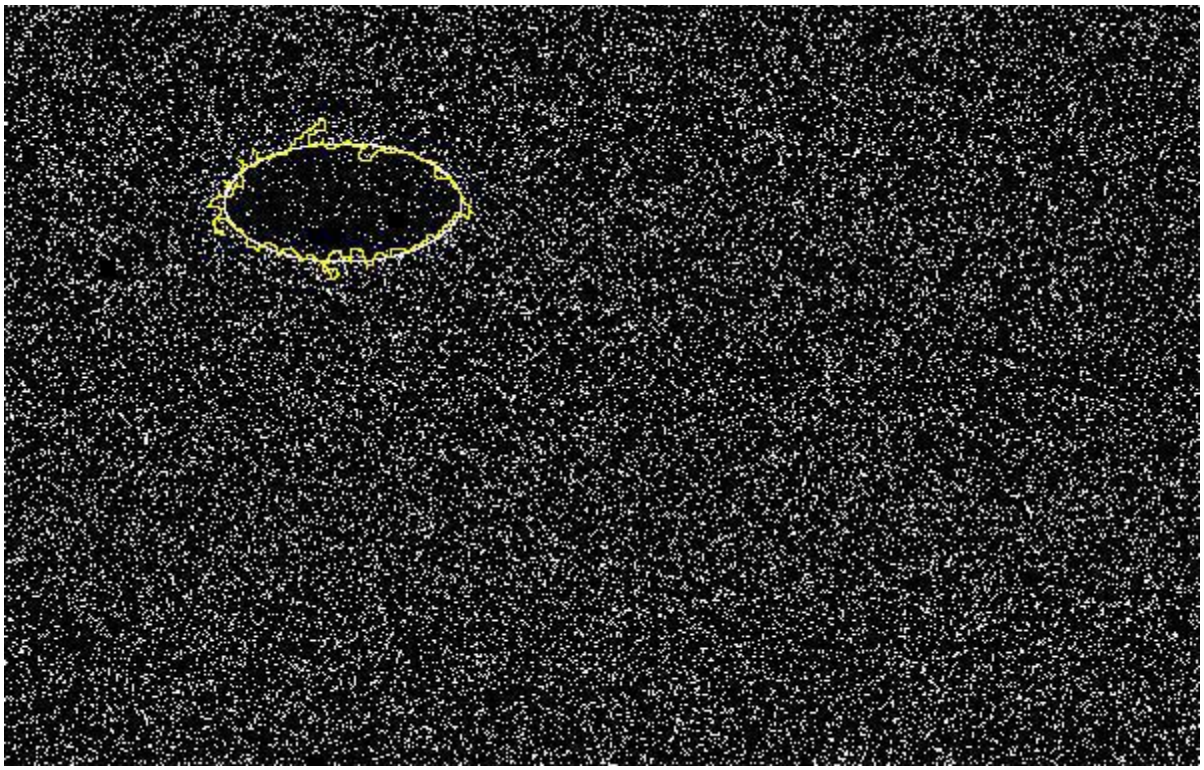

(b)

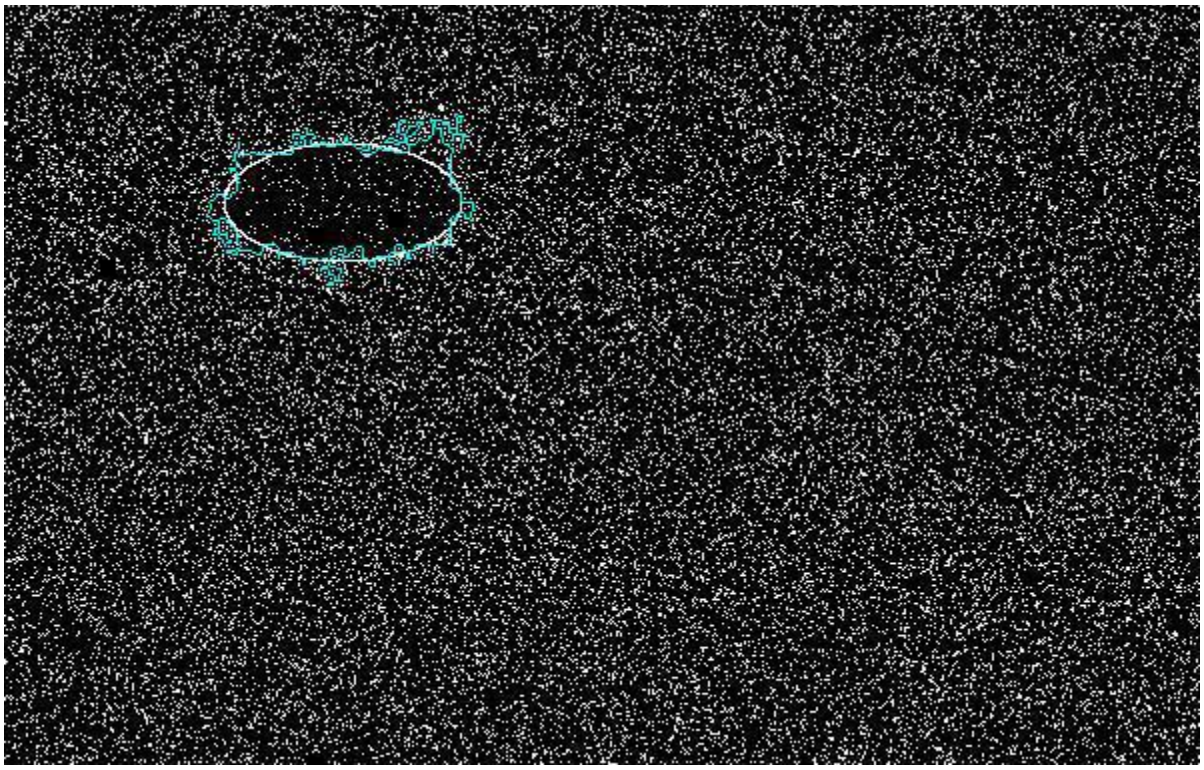

(c)Figure 5: A designated simulation image (a), the result of PES segmentation (b), and the result of Region Growing segmentation

The simulation repeats for 1000 times. The total number of pixels in the designated ROI is 5641. After the algorithm classifies the pixels in the ROI, it compares the result with the designated image to calculate the accuracy of the algorithm. Within the 1000 times simulation, PES classifies 5819 pixels as elements of ROI with standard deviation of 198 pixels, while region growing classifies 6407 as elements of ROI with standard deviation of 313 pixels. Out of all pixels classified as part of ROI, the mean accuracy of PES is 91.28% with the standard deviation of 1.97% while the mean accuracy of region growing is 83.59% with the standard deviation of 3.45%. In addition, PES spends 2077 seconds to finish 1000 times simulation while region growing spends 4259 seconds to complete the same task. Therefore, PES has not only better accuracy than region growing, but also higher efficiency.

4.8 Conclusion

PES shows promising performance through the above evaluation. The multiple statistical features of the algorithm improve the robustness of the performance of the algorithm and reduce the influence of inconsistent speckles and noise commonly associated with ultrasound images. There are many possibilities for enhancement of the basic algorithm, since it is easy to build a test to see if a given feature is redundant or if a candidate new feature is promising. The projection step of PES which combines motion estimation of the biomedical ultrasound video and the ROI in each frame efficiently estimates the approximate location of internal region in the succeeding frame and removes any requirement for manual intervention in succeeding frames. Unlike most segmentation algorithms, PES approaches the image from a global perspective by comparing the statistical feature differences between the internal region and the external region to retrieve empirical ROI. Furthermore, the algorithm preserves the empirical value of the current frame and projects them onto the succeeding frame which helps prevent degradation due to poor image quality. The PES approach was developed and demonstrated herein. Its performance in the above applications suggests that the PES method could be a useful tool to aid in clinical and scientific evaluation of B-mode, cine ultrasound images.

5 Quantitative Ultrasound

5.1 Introduction

Biomedical ultrasound is a prominent imaging modality for diagnostics.

Conventional ultrasonic imaging is qualitative in nature with spatial resolution up to hundreds of micrometers. Quantitative ultrasound techniques based on ultrasonic backscatter can provide estimates describing tissue microstructure. Improving quantitative ultrasound techniques will result in improved diagnostic capabilities of ultrasound.

Quantitative techniques were developed and assessed based on the envelope of backscattered ultrasound. The envelope of backscattered ultrasound can be modeled as the superposition of the scattered signals from individual scatterers in the medium being interrogated. As such, the envelope signal is statistical in nature. By applying a model to the amplitude distribution of the envelope, information about the sub-resolution material properties such as the scatterer number density and organizational structure can be obtained.

The Homodyned K distribution and the Nakagami distribution was used to model the envelope of backscattered ultrasound. An efficient parameter estimation algorithm was developed and tested through simulations and experiments. Techniques to reduce estimate bias and variance were assessed. The diagnostic potential of tissue characterization based on envelope statistics was evaluated.

5.2 Basic Functionalities

Both the method uses different approach to characterize the propagation media, in this case the propagation media is live tissue. The characterization of the propagation media is done with parametric values from this two distribution. Homodyne k provides us with information about scattered density per resolution cell and energy ratio. Nakagami distribution gives us information about effective number of scatterer and effective cross section area of scatterer. Computing these parameters for inside and outside of the region of interest (ROI) provides us with different numerical values. These values might help to distinguish between types of tissues.

5.3 Background and Motivation

Breast ultrasound is being proposed as an adjunct to x-ray mammography to aid in the reduction of unnecessary biopsies associated with mammography ([61], [62], [63], [64]).

Ultrasound (US) also has been recommended to detect and diagnose masses in patients with radiologically dense breast tissue. Thus, there is an increased interest in the use of US in breast cancer diagnosis. The interpretation of US images is undertaken by trained radiologists who use a number of visual features such as texture, shape of the mass, boundary characteristics, posterior shadow, echo structure, etc, to diagnose the mass. Thus, these diagnostic decisions are strongly influenced by the training and experience of the radiologist. They are also influenced by the manner in which the images were collected, i.e., they may be operator and machine dependent ([65]). It is therefore potentially useful to have an automated classification scheme requiring minimal clinical intervention that relies heavily on machine computed parameters ([66]).

These automated techniques have to rely on features that are characteristic of the backscattered echo from the breast tissue. Efforts have been made to undertake the classification of breast masses using the spectral characteristics of the backscattered echo([67]). Some success has also been achieved by decomposing the echo into diffuse and coherent components and constructing parameters that reflect these components ([68]). Parameters of the density functions of the envelope of the backscattered echo have also been used in the breast mass classification ([69], [70]). The efforts by our group involved the use of the K distribution and later the use of the Nakagami distribution for the classification ([69], [70]). Parameters of these density functions were used to discriminate between benign and malignant masses. Additional efforts were made by combining a few features of the mass ([71]) leading to enhancement in the performance in terms of a higher area (*Az*) under the receiver operating characteristic curve (ROC). While the K and Nakagami distributions are reasonable ways of modelling the echo of the backscattered envelope, their parameters have somewhat different relationships to the scattering conditions in the tissue.

This diversity existing within the models (K and Nakagami distributions) can be utilized to enhance the breast mass classification taking the performance levels to match or exceed those of conventional x-ray mammography. Such an effort is undertaken in this work. In the present work, parameters of the Nakagami and K distributions were extracted and fused to form a new discriminant. In addition, a few other parameters of the image derived from the boundary of the mass, posterior shadow and texture were added to this new discriminant ([72], [62]). These parameters, extracted with minimal clinical intervention, were studied for their performance to enhance the area under the ROC curve.

5.4 Overview

We propose on using three parameters for mass classification, (i) The “k” parameter for Homodyned K distribution (ii) The “m” parameter of Nakagami distribution (iii) The Roughness parameter

5.5 Homodyned K distribution

5.5.1 Envelop Statistics Model

A number of models for the statistics of the envelope of acoustic and optical signals have been proposed over the past few decades with applications to sea echo [73], medical ultrasound [74], and laser [75]. Some of these distributions include the Rayleigh distribution, the K distribution, and the homodyned K distribution. Because the derivations of these distributions have been covered extensively in the literature (e.g., [76], [77]), only a brief review is given.

5.5.2 Rayleigh distribution

The Rayleigh distribution arises when a large number of nearly identical and randomly located scatterers contribute to the echo signal . The probability density function (pdf) is given by

$$p_A(A) = \frac{A}{\sigma^2}\exp\left(-\frac{A^2}{2\sigma^2}\right)$$

where *A* (which is assumed to be positive) represents the envelope amplitude and 2sigma squared is the variance of the Gaussian distributed in-phase and quadrature components of the complex echo envelope.

5.5.3 K distribution

Jakeman and Pusey [73] introduced the use of the K distribution, a generalization of the Rayleigh distribution, in the context of microwave sea echo to model situations where the number of scatterers is not assumed to be large. The pdf is given by

$$p_A(A) = \frac{2b}{\Gamma(\mu)}\left(\frac{bA}{2}\right)^{\mu} K_{\mu-1}(bA)$$

where $\Gamma(\bullet)$ is the Gamma function, $(\ )_n K \bullet$ is the modified Bessel function of the second kind, *n*-th order, and μ is a measure of the effective number of scatterers per resolution cell. In ultrasound, the resolution cell volume can be defined as the volume of the point spread function of the imaging system [15], i.e., the volume of the insonifed medium that contributes to any given point in the echo signal. In Equation above, the *b* parameter can be expressed as

$$b = 2\sqrt{\frac{\mu}{E\left[A^2\right]}}$$

where $E[\bullet]$ is the expectation operator. The K distribution is a more general model that approaches the Rayleigh distribution in the limit $\mu \to \infty$ [14].

5.5.4 Homodyned K distribution

The homodyned K distribution was first introduced by Jakeman [78]. Besides incorporating the capability of the K distribution to model situations with low effective scatterer number densities, the homodyned K distribution can also model situations where a coherent signal component exists due to periodically located scatterers [77]. This makes the homodyned K distribution the most versatile of the three models discussed, but also the most complicated. The pdf of the homodyned K distribution does not have a closed form expression; however, it can be expressed in terms of an improper integral as

$$p_A(A) = A\int_0^\infty xJ_0(sx)J_0(Ax)\left(1+\frac{x^2\sigma^2}{2\mu}\right)^{-\mu} dx$$

where $J_0(\bullet)$ is the zeroth order Bessel function of the first kind, s^2 is the coherent signal energy, σ^2 is the diffuse signal energy, and μ is the same as in the K distribution. The derived parameter $k = s/\sigma$ is the ratio of the coherent to diffuse signal and can be used to describe the level of structure or periodicity in scatterer locations. The pdf can also be expressed in terms of the Rice and Gamma distributions [76]

$$p_A(A) = \int_0^\infty p_R(A \mid z)\, p_\gamma(z)\, dz$$

Here $p_R(A \mid z)$ is the Rice distribution with scale parameter σz /μ and non centrality parameter *s* whose pdf given by

$$p_R(A \mid z) = \frac{A\mu}{\sigma^2 z} \exp\left(-\frac{\mu\left(A^2 + s^2\right)}{2\sigma^2 z} \right) I_0\left(\frac{sA\mu}{\sigma^2 z} \right)$$

where $I_0(\bullet)$ is the zeroth order modified Bessel function of the first kind and $p_\gamma(z)$ is the Gamma distribution with shape parameter μ and scale parameter unity. The pdf of the Gamma distribution with these parameters is given by [10]

$$p_\gamma(z) = \frac{z^{\mu-1} e^{-z}}{\Gamma(\mu)}$$

The pdf of the homodyned K distribution can further be expressed as an infinite summation (using the form given by [17], expressing the pdf in terms of the parameters used in Equation (1.4), and simplifying),

$$p_A(A) = \sum_{n=0}^{\infty} \frac{\frac{2\mu A}{\sigma^2}}{\Gamma(\mu)(n!)^2} \left(\frac{\mu s A}{2\sigma^2} \right)^{2n} \left(\frac{1}{\sigma} \sqrt{\frac{\mu\left(s^2 + A^2\right)}{2}} \right)^{\mu-1-2n} K_{2n+1-\mu}\left(\frac{1}{\sigma} \sqrt{2\mu\left(s^2 + A^2\right)} \right)$$

The series is convergent except for the case when both μ <1/ 2 and $A = s$. The form given by Equation (1.8) is especially useful for numerically computing values of the pdf as it is usually possible to quickly obtain a good approximation of the pdf by considering only a small, finite number of terms in the infinite summation. The accuracy of the approximation depends on the particular parameter values for which the series is evaluated. In general, the rate of convergence is

slower when the parameters are closer to the case where the series does not converge at all (i.e., $\mu < 1/2$ and $A = s$). Figure 1.1 shows four examples of the relative truncation error (the truncation error divided by

actual pdf value) versus the number of terms considered in the truncated series. To validate the approximation for a particular set of parameter values, the pdf can be sampled for values of A on the interval $[0, a]$ where a is chosen to be sufficiently large such that $p(A)$ is negligible on the tail of the distribution $(a, \infty]$. Then, numerical integration can be performed on the sampled pdf. As the pdf should integrate to unity, if the result of numerical integration differs substantially from unity, the accuracy of the approximation is questionable, suggesting that more terms are needed to obtain a good approximation.

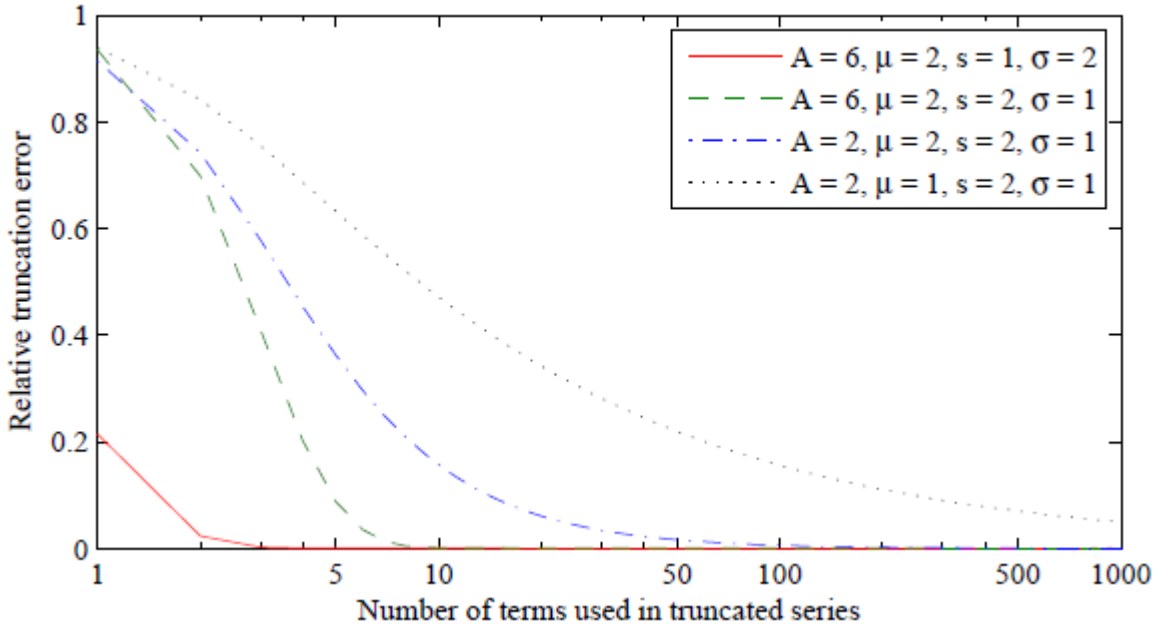

Figure: Relative truncation error versus the number of terms used in the truncated series

The homodyned K distribution model has been criticized (e.g., [69], [79], [80]) because of its analytical complexity. Hence, its use has been somewhat limited and other, more analytically tractable models such as the Nakagami distribution, Weibull distribution, Rician inverse Gaussian distribution, and generalized gamma distribution have been used instead. Because the homodyned K distribution is both versatile and analytically complex, a goal of this work is to develop and apply methods to reduce the impact of this complexity while retaining the benefits of the versatility. By improving existing parameter estimation techniques, accurate parameter estimates can be obtained quickly. An improved parameter estimation algorithm will also provide more accurate information to better elucidate the relationships between the envelope statistics

and the underlying structures responsible for the signals. Furthermore, as a by-product of the estimation algorithm, a geometrical interpretation into modeling of the envelope of backscattered ultrasound using the homodyned K distribution can be obtained.

5.5.5 Nakagami Distribution

When an acoustic pulse travels through tissue, the backscattered echo may be modeled as the algebraic sum of the contributions from the individual scatterers [74], [77]. If there are N scatterers in the range cell, and *an* and *_n* represent the amplitude and the phase of the nth scatterer, respectively, the backscattered echo may be written as:

$$s(t) = \sum_{n=1}^{N} a_n \cos(\omega_0 t - \theta_n)$$

where *!*0 = 2_*f*0, *f*0 is the center frequency of insonation. The backscattered echo *s*(*t*) also can be written in terms of the inphase and quadrature components, X and Y, respectively, as:

$$s(t) = X\cos(\omega_0 t) + Y\sin(\omega_0 t)$$

Where

$$X = \sum_{n=1}^{N} a_n \cos(\theta_n) \text{ and } Y = \sum_{n=1}^{N} a_n \sin(\theta_n).$$

The envelope of the backscattered echo, R, is given by:

$$R = \sqrt{X^2 + Y^2}\ .$$

The number density of scatterers *N* and the location of the scatterers play an important role in describing the statistics of the envelope of the backscattered echo. If the range cell contains a large number of randomly located scatterers, the central limit theorem can be invoked, due to which *X* and *Y* would be Gaussian distributed with zero mean and equal variance. The envelope *R* under this condition

will obey Rayleigh statistics. The phase arctan(Y/X) will be uniform in the range 0 to 2_. If the range cell

contains scatterers that have randomly varying scattering cross sections with a comparatively high degree of variance, it was shown [77] that the Rayleigh statistics might not hold. In such cases, the inphase and quadrature components of the backscattered echo from tissue do not follow Gaussian statistics. The envelope statistics are pre-Rayleigh [76], [77]. However, if the range cell

contains periodically located scatterers at spacings corresponding to integral multiples of the wavelength at the frequency of demodulation or integral multiples of half the wavelength corresponding to the demodulation frequency in addition to randomly located scatterers, the

inphase and quadrature components of the backscattered echo are Gaussian with equal variance but unequal mean. The envelope statistics under these conditions are Rician or post-Rayleigh [78].

All these scattering conditions exist in radar and the Nakagami distribution can encompass all these scattering conditions. The Nakagami probability density function *f*(*r*), is given as:

$$f(r) = \frac{2m^m r^{2m-1}}{\Gamma(m)\Omega^m} \exp(-\frac{m}{\Omega} r^2) U(r).$$

In (4) □( ) is the Gamma function and *U*( ) is the unit step function. The cumulative distribution of the Nakagami distributed envelope *F*(*r*) is given by:

$$F(r) = \int_0^r \frac{2m^m x^{2m-1}}{\Gamma(m)\Omega^m} \exp\left(-\frac{m}{\Omega} x^2\right) dx = P\left(\frac{m}{\Omega} r^2, m\right)$$

where *P*(*: ; :*) is the incomplete Gamma function.This distribution has two paramaters, namely, *m* and omega. They are estimated as:

$$m = \frac{\left[E\left(R^2\right)\right]^2}{E\left[R^2 - E\left(R^2\right)\right]^2}$$

$$\Omega = E(R^2)$$

where *E*( ) stand for statistical average. The parameter *m* is referred to as the Nakagami parameter and is constrained such that m is greater than or equal to 0.5. The quantity m is a shape

parameter and conveys information about the envelope statistics. The parameter omega is a scaling parameter. The parameter that we will be using for classification is the m parameter.

5.5.6 Roughness

The boundary coordinates of the lesion is obtained from the image segmentation. The roughness parameter is basically a measure of the variance of the distance of the boundary coordinates from the centroid.

The malignant masses is known to have a rough zigzag boundary and hence the variance in the distance of the boundary coordinates is expected to be greater for malignant tumors.

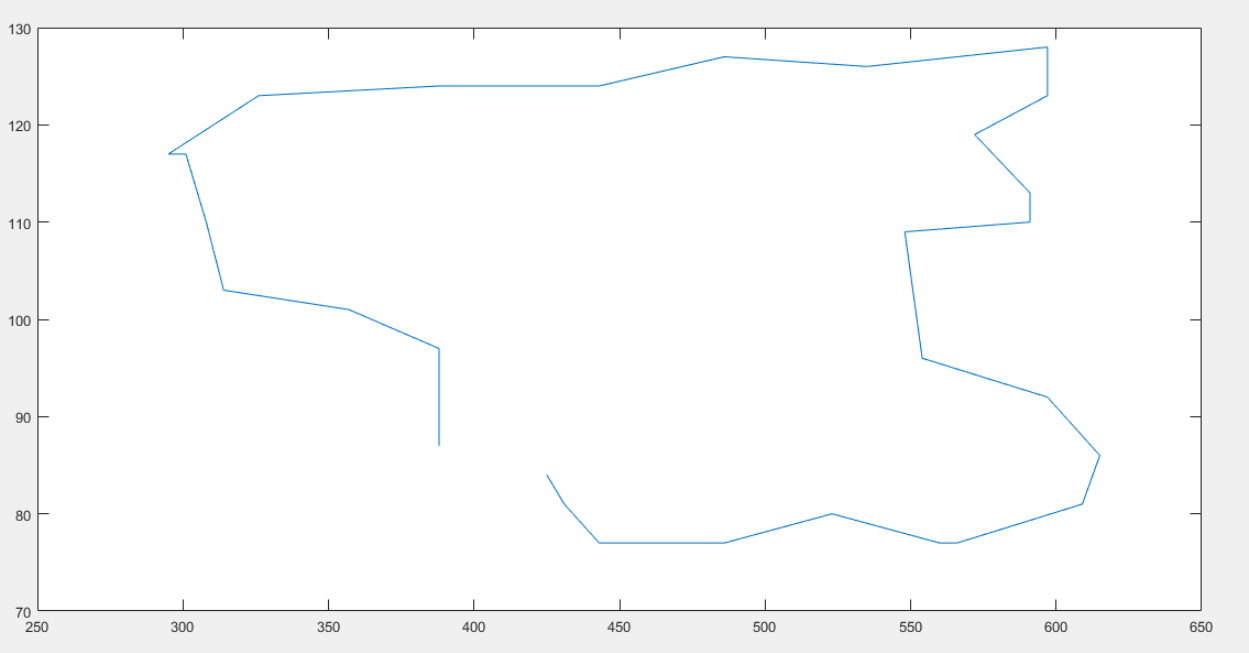

Figure: The boundary of a malignant tumor

Benign tumors on the other hand is known have much smoother boundary condition compared to malignant tumors. Hence the variance in the distance of boundary coordinates from the centroid is likely to be lower.

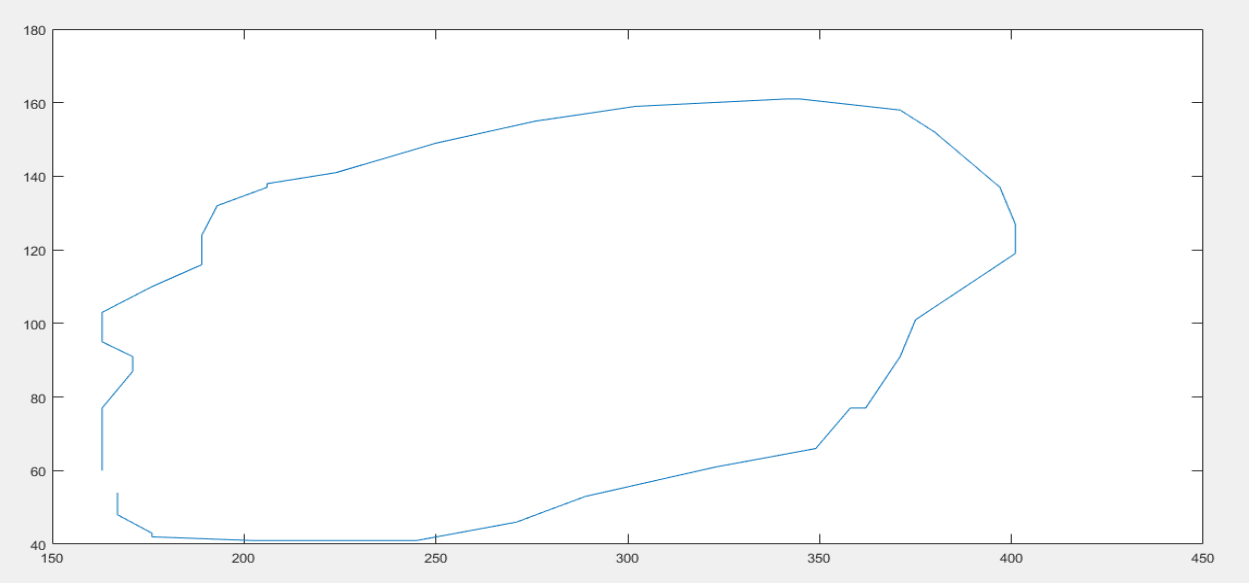

Figure: The boundary of a benign tumor

5.6 Process and Results

From the image segmentation we will be getting the boundary coordinates of the lesion. Using the boundary coordinates we will be isolating our Region of Interest(ROI) and perform the parameter calculations.

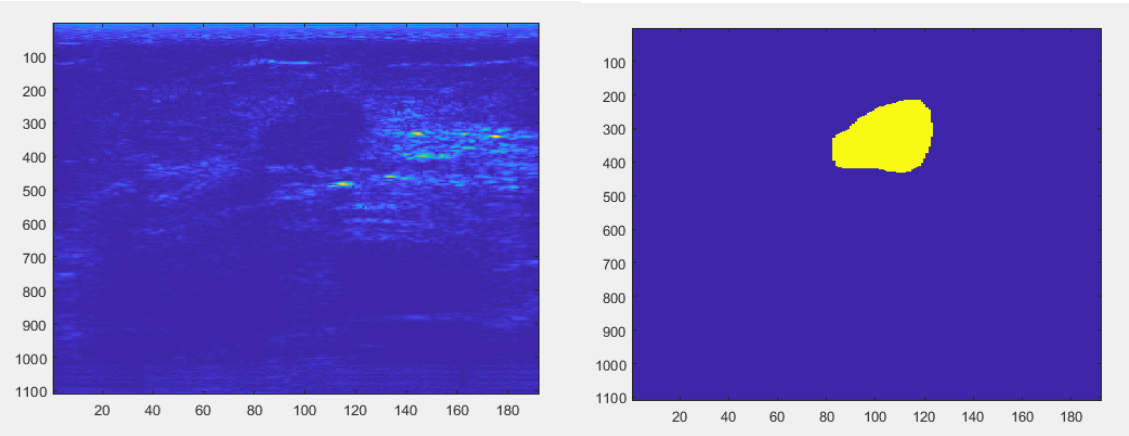

(a) (c)

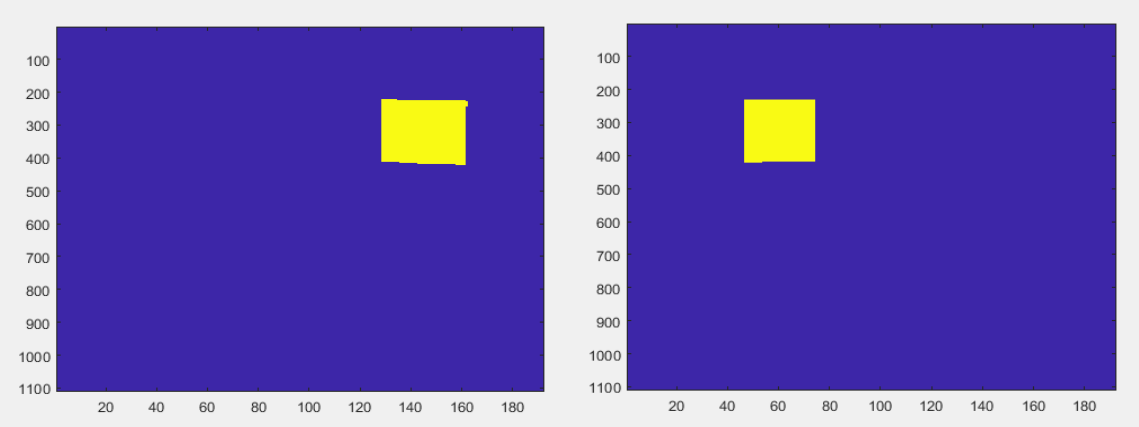

(b) (d)

Figure: (a) The B-mode image of a patient (b) The right lateral region of the tumor (c) The tumor (d) The left lateral region

For our parameter calculation we have taken three regions of interest, the tumor, the left lateral and the right lateral region. The three ROIs are at the same depth so that the results are free from any depth dependent effects.

5.7 K parameter calculation of Homodyned k distribution

In this method we try to find the correlation between RSK values. From our back scatter Signal we will calculate the RSK values (slew rate, kurtosis, signal to noise ratio),finding the correlation from the precompiled values of RSK , homodyne k values are found. Martin-Fernandez et al. [81] first introduced an estimation methodology for the homodyned K distribution using level sets; however, the algorithm was based on only the SNR. The present estimation algorithm contains several incremental improvements over this initial idea, most notably the extension to include skewness and kurtosis.

Fundamentally, parameter estimates are obtained by following the procedure outlined in Figure 2.1 and equating theoretical values for the nonparametric classifiers.

For a fixed moment order, n , the nonparametric classifiers are functions of two variables. Therefore, given an estimate of a nonparametric classifier, it is possible to map out a curve of possible parameter values (a level curve) in two dimensions. Such an example is shown in subplot (a) in Figure below. By considering a second classifier function, a second level curve can be drawn (subplot (b) in Figure below). Because there are two unknown model parameters, two classifier functions should uniquely identify a parameter estimate because their level curves should intersect at one point. However, for improved robustness, three classifier functions are used (subplot (c) in Figure below) resulting in an overdetermined system. Furthermore, level curves using a number of different moment orders can be used, resulting in a further overdetermined system.

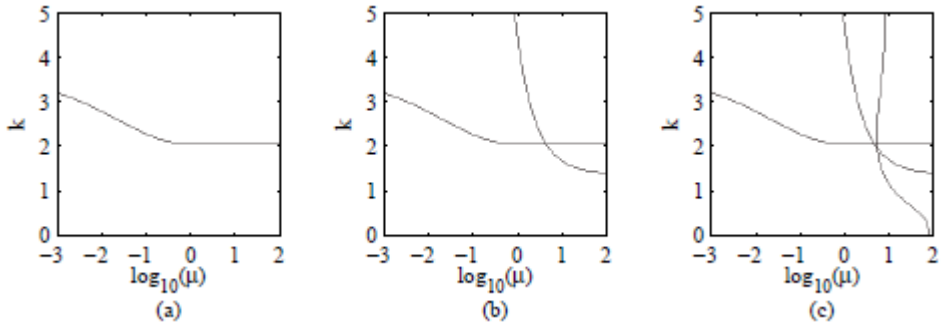

Figure: Examples of level curves using moment order v=1 for (a) SNR, (b) SNR and skewness, and (c) SNR, skewness, and kurtosis. Intended parameter values: k=2 and log10(mu) = 0.7

5.8 m parameter calculation of Nakagami distribution

The m parameter was calculated both inside and outside the lesion. For calculation outside the lesion we calculate the parameters for both the left and right lateral regions and take the average to get one single value of m outside the lesion.

5.9 Roughness parameter

From the boundary coordinates we calculate the centroid of the lesion. Then we calculate the distance of each of the boundary coordinates from the centroid and store this value in a single vector. Variance of this vector will give a measure of boundary roughness.

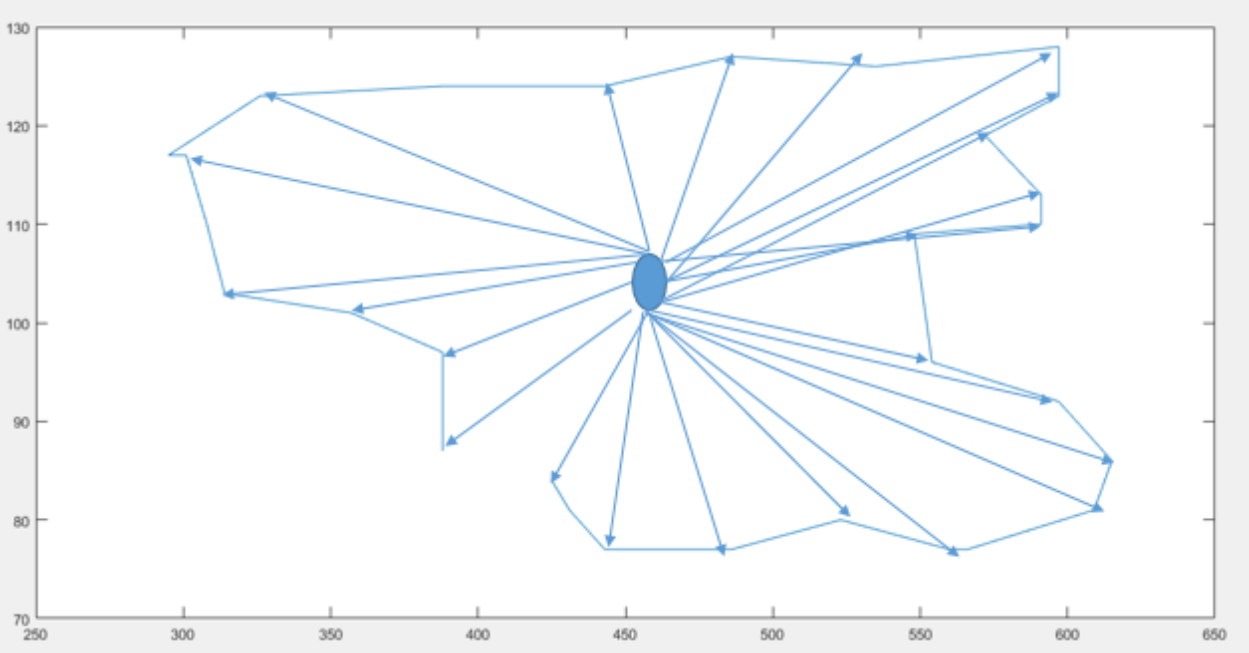

For our classification we have used the linear discriminant analysis(LDA) in Matlab. This classification tool helps in classification between two or more classes. The classes in our case was benign or malignant. We ran our code on 130 patient data sets out of which 100 patients were benign and 30 were malignant. From the results obtained we performed the LDA and saw the a clear distinction in the results. There was clear division between benign(B) and malignant(M) regions with little bit of overlapping.

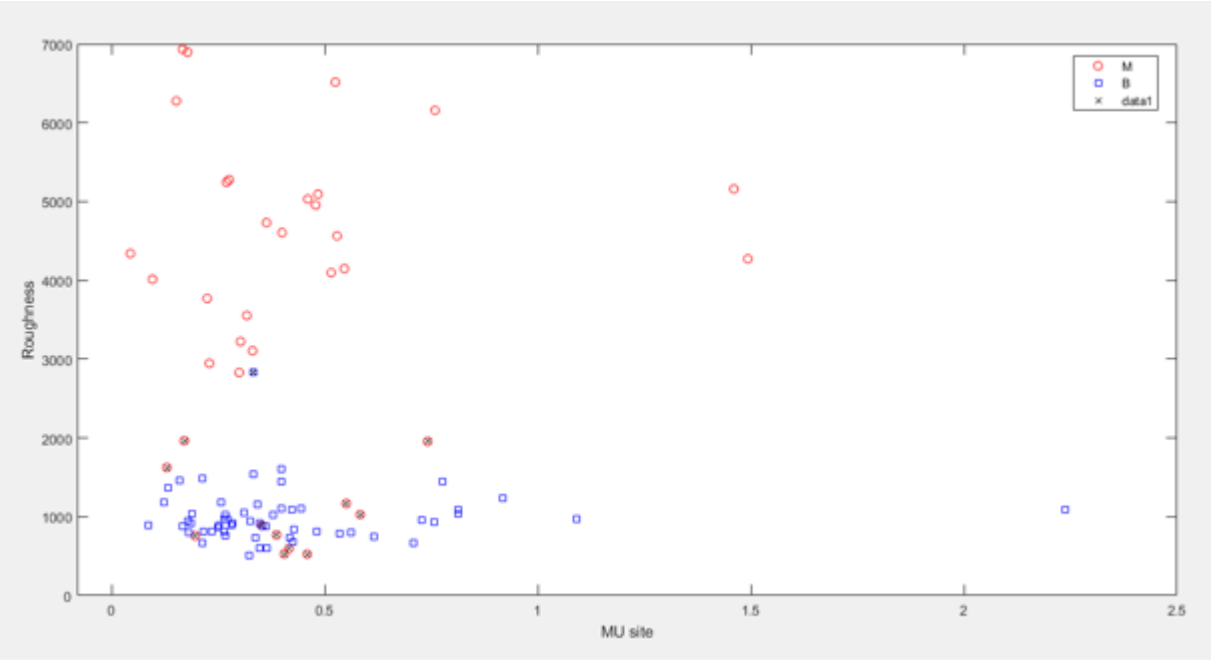

Figure: LDA of Roughness against “m” parameter in tumor

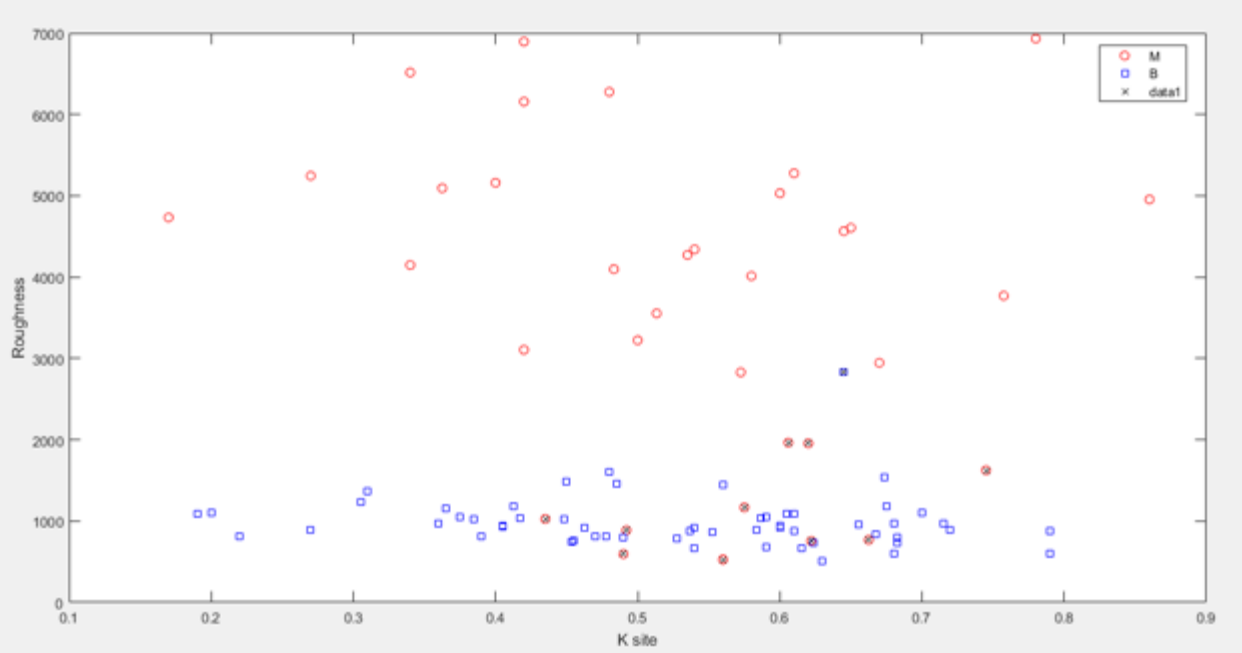

Figure: LDA of Roughness against “K” parameter in tumor

6.Future scope

Integration of these three approaches on GPU based machines for faster computation.

7. Conclusion

This classification tool helps in classification between two or more classes. The classes in our case was benign or malignant. We ran our code on 130 patient data sets out of which 100 patients were benign and 30 were malignant. From the results obtained we performed the LDA and saw a clear distinction in the results. There was clear division between benign(B) and malignant(M) regions with little bit of overlapping. The LDA showed an 81.3% accuracy in distinguishing benign from malignant tumors in our data set.

8. References

1 H. Cheng, J. Shan, W. Ju, Y. Guo, and L. Zhang, "Automated breast cancer detection and classification using ultrasound images: A survey," Pattern Recognition, vol. 43, pp. 299-317, 2010.

2 R. L. Siegel, K. D. Miller, and A. Jemal, "Cancer statistics, 2016," CA: a cancer journal for clinicians, vol. 66, pp. 7-30, 2016.

3 M. P. Coleman, M. Quaresma, F. Berrino, J.-M. Lutz, R. De Angelis, R. Capocaccia, et al., "Cancer survival in five continents: a worldwide population-based study (CONCORD)," The lancet oncology, vol. 9, pp. 730-756, 2008.

4 C. Society, "Cancer Facts & Figures 2016," American Cancer Society; 2016, Atlanta2016.

5 K. M. Kelly, J. Dean, W. S. Comulada, and S.-J. Lee, "Breast cancer detection using automated whole breast ultrasound and mammography in radiographically dense breasts," European radiology, vol. 20, pp. 734-742, 2010.

6 S. Shapiro, W. Venet, P. Strax, L. Venet, and R. Roeser, "Ten-to fourteen-year effect of screening on breast cancer mortality," Journal of the National Cancer Institute, vol. 69, pp. 349-355, 1982.

7 Jalalian, S. B. Mashohor, H. R. Mahmud, M. I. B. Saripan, A. R. B. Ramli, and B. Karasfi, "Computer-aided detection/diagnosis of breast cancer in mammography and ultrasound: a review," Clinical imaging, vol. 37, pp. 420-426, 2013.

8 R.-F. Chang, W.-J. Wu, W. K. Moon, and D.-R. Chen, "Improvement in breast tumor discrimination by support vector machines and speckle-emphasis texture analysis," Ultrasound in medicine & biology, vol. 29, pp. 679-686, 2003.

9 J. Shan, H. Cheng, and Y. Wang, "A novel segmentation method for breast ultrasound images based on neutrosophic l-means clustering," Medical physics, vol. 39, pp. 5669-5682, 2012.
10 B. Sahiner, H.-P. Chan, M. A. Roubidoux, L. M. Hadjiiski, M. A. Helvie, C. Paramagul, et al., "Malignant and Benign Breast Masses on 3D US Volumetric Images: Effect of Computer-aided Diagnosis on Radiologist Accuracy 1," Radiology, vol. 242, pp. 716-724, 2007.
11 K. Drukker, M. L. Giger, K. Horsch, M. A. Kupinski, C. J. Vyborny, and E. B. Mendelson, "Computerized lesion detection on breast ultrasound," Medical physics, vol. 29, pp. 1438-1446, 2002.
12 Y.-L. Huang, D.-R. Chen, and Y.-K. Liu, "Breast cancer diagnosis using image retrieval for different ultrasonic systems," in Image Processing, 2004. ICIP'04. 2004 International Conference on, 2004, pp. 2957-2960.

13 W. Gómez-Flores and B. A. Ruiz-Ortega, "New Fully Automated Method for Segmentation of Breast Lesions on Ultrasound Based on Texture Analysis," Ultrasound in medicine & biology, vol. 42, pp. 1637-1650, 2016.
14 Madabhushi and D. N. Metaxas, "Combining low-, high-level and empirical domain knowledge for automated segmentation of ultrasonic breast lesions," IEEE transactions on medical imaging, vol. 22, pp. 155-169, 2003.
15 S. K. Alam, E. J. Feleppa, M. Rondeau, A. Kalisz, and B. S. Garra, "Ultrasonic multi-feature analysis procedure for computer-aided diagnosis of solid breast lesions," Ultrasonic imaging, vol. 33, pp. 17-38, 2011.
16 P. H. Arger, C. M. Sehgal, E. F. Conant, J. Zuckerman, S. E. Rowling, and J. A. Patton, "Interreader variability and predictive value of US descriptions of solid breast masses: pilot study," Academic radiology, vol. 8, pp. 335-342, 2001.
17 B. Liu, H. Cheng, J. Huang, J. Tian, J. Liu, and X. Tang, "Automated segmentation of ultrasonic breast lesions using statistical texture classification and active contour based on probability distance," Ultrasound in medicine & biology, vol. 35, pp. 1309-1324, 2009.
18 T. A. Krouskop, D. R. Dougherty, and F. S. Vinson, “A pulsedDoppler ultrasonic system for making noninvasive measurements of the mechanical properties of soft tissue,” J. Res.Dev., vol. 24, pp. 1–8, 1987.
19 R. M. Lerner and K. J. Parker, “Sono-elasticity in ultrasonic tissue characterization and echographic imaging,” inProc. 7th Eur. Comm. Workshop, J. M. Thijssen, Ed. Nijmegen, The Netherlands, 1987.
20 R. M. Lerner, S. R. Huang, and K. J. Parker, “‘Sonoelasticity’images derived from ultrasound signals in mechanically vibrated tissues,” Ultrason. Med. Biol., vol. 16, pp. 231–239, 1990.

21 Y. Yamakoshi, J. Sato, and T. Sato, “Ultrasonic imaging of internal vibration of soft tissue under forced vibration,” IEEE Trans. Ultrason., Ferroelect., Freq. Contr., vol. UFFC-47,45–53, 1990.
22 J. Ophir, I. C´ espedes, H. Ponnekanti, Y. Yazdi, and X. Li, “Elastography: A method for imaging the elasticity in biological tissues,” Ultrason. Imaging, vol. 13, pp. 111–134, 1991.
23 M. O’Donnell, A. R. Skovoroda, B. M. Shapo, and S. Y. Emelianov, “Internal displacement and strain imaging using ultrasonic speckle tracking,” IEEE Trans. Ultrason., Ferroelect.,
Freq. Contr., vol. UFFC-41, pp. 314–325, 1994.
24 S. K. Alam, D. W. Richards, and K. J. Parker, “Detection of intraocular pressure change in the eye using sonoelastic Doppler ultrasound,” Ultrason. Med. Biol., vol. 20, pp. 751–758, 1994.

25 K. J. Parker, L. Gao, R. M. Lerner, and S. F. Levinson, "Techniques for elastic imaging: A review,"IEEE Engineering in Medicine and Biology Magazine, vol. 15, no. 6, pp. 52–59, 1996.
26 S. K. Alam, J. Ophir, and E. E. Konofagou, "An adaptive strain estimator for elastography," IEEE Transactions on Ultrasonics, Ferroelectrics and Frequency Control, vol. 45, no. 2,461–472, Mar. 1998
27 Wells, P. N. T. (June 2011). "Medical ultrasound: imaging of soft tissue strain and elasticity". Journal of the Royal Society, Interface. 8 (64): 1521–1549. doi:10.1098/rsif.2011.0054. PMC 3177611.
28 J. Ophir, I. C´espedes, H. Ponnekanti, Y. Yazdi, and X. Li, "Elastography: A method for imaging the elasticity in biological tissues," Ultrason. Imaging, vol. 13, pp. 111-134, 1991.
29 Brusseau E, Perrey C, Delachartre P, Vogt M, Vray D, Ermert H. Axial strain imaging using a local estimation of the scaling factor from RF ultrasound signals. Ultrason Imaging 2000;22:95–107.
30 Doyley MM, Mastik F, De Korte CL, Carlier SG, Cespedes EI,Serruys PW, Bom N, Van der Steen AFW. Advancing intravascular ultrasonic palpation toward clinical applications.
31 Kallel F, Bertrand M. Tissue elasticity reconstruction using linearperturbation method. IEEE Trans Medl Imaging 1996;15:299–313.
32 Zhu Y and Hall T J 2002 A modified block matching method for real-time freehand strain imaging Ultrason. Imaging
33 Garra BS. Imaging and estimation of tissue elasticity by ultrasound.Ultrasound Q 2007;23:255–268.
34 Kallel F, Ophir J, Magee K, Krouskop T. Elastographic imaging of lowcontrast elastic modulus distributions in tissue. Ultrasound Med Biol 1998;24:409–425.

35 H. Shi and T. Varghese,“Two-dimensional multi-level strain estimation for discontinuous tissue,” Phys. Med. Biol. 52, 389–401 2007.
36 J. Shan, H. Cheng, and Y. Wang, "Completely automated segmentation approach for breast ultrasound images using multiple domain features," Ultrasound in medicine & biology, vol. 38, pp.262-275, 2012
37 Ardeshir Goshtasby: 2-D and 3-D Image Registration for Medical, Remote Sensing, and Industrial Applications, Wiley Press, 2005.
38 Rashid Al Mukaddim, Juan Shan, Irteza Enan Kabir, Abdullah Salmon Ashik, Rasheed Abid, Zhennan Yan,
39 Dimitris N. Metaxas, Brian S. Garra, Kazi Khairul Islam1 and S. Kaisar Alam, "A Novel and Robust Automatic Seed Point Selection Method for Breast Ultrasound Images."

40 Kobayashi, H. and Vanderby, R.,2007,” Acoustoelastic analysis of reflected waves in nearly incompressible,hyper-elastic materials: Forward and inverse problems,” J. Acoust..Soc. Am.,Vol.121 (2), pp.879-887
41 Kobayashi, H., Wu, M.J, Kaplan, LD and Vanderby, R,” APPLICATION OF ACOUSTO-ELASTICITY TO NONINVASIVE TISSUE STRAIN MEASUREMENT”, 53rd Annual meeting of Orthopaedic Research Society, February (2007)
42 Kobayashi, H. and Vanderby, R.,2010,” Strain and stiffness measurements in stretched soft tissues based on acoustoelasticity- a new ultrasound technique“ Submitted to Journal of Biomchanics
43 T. Tuthill, J. Rubin, J. Fowlkes, D. Jamadar, R. Bude, “Frequency Analysis of Echo Texture in Tendon”, Ultrasound in Medicine & Biology, Volume 25, Issue 6, July 1999, Page 959-968
44 A. Meghoufel, G. Cloutier, N. Crevier-Denoix, J.A. De Guise, J.A.,“A thinning algorithm for equine tendon structure identification from 2D ultrasound images”, Biomedical Imaging: From Nano to Macro, 2008. ISBI 2008. 5th IEEE International Symposium on 14-17 May 2008, Page 1565-1568
45 Y.L. Huang, D.R.Chen , “Watershed Segmentation for Breast Tumor in 2-D Sonography”, Ultrasound in Medicine & Biology, May 2004, Volume 30, Issue 5, Pages 625-632
46 M. Kass, A. Witkin, D. Terzopoulos, “Snakes: Active Contour Models”, International Journal of Computer Vision, Vol: 4, Num: 4, January 1998, Page 321-331.
47 C. Xu, J. Prince, “Snakes, Shapes, and Gradient Vector Flow”, IEEE Transactions on Image Processing, Vol. 7, No. 3, March 1998, Page 359-369
48 M.A. Sutton, W.J. Wolters, W.H. Peters, W.F. Ranson, S.R. McNeill, “Determination of displacements using an improved digital correlation method”, Image and vision computing, [0262-8856] Sutton 1983, Vol:1, Iss:3, Page 133.
49 T.C. Chu, W.F. Ranson, M.A. Sutton, W.H. Peters, “Applications of digital image correlation techniques to experimental mechanics”, Exp Mech 25 (1985), 232.
50 H.A. Bruck, S.R. McNeill, M.A. Sutton, W.H. Peters III, “Digital image correlation using Newton-Raphson method of partial differential correction”, Exp Mech 29 (1989) 261.

51 R. O. Duda, P. E. Hart, and D. G. Stork, *Pattern Classification*, 2cnd Edition, John Wiley and Sons, 2001.

52 R. C. Gonzales and R. E. Woods , *Digital Image Processing*, 3rd Edition, Prentice Hall, 2008.

53 H. Guan; D.Y Li; J.L. Lin; T.F. Wang, "Segmentation of Ultrasound Medical Image Using A Hybrid Method", IEEE/ICME International Conference on Complex Medical Engineering, 2007. CME 2007, May 2007 Page 644-647

54 A. Thakur, R. S. Anand, " A Local Statistics Based Region Growing Segmentation Method for Ultrasound Medical Images", International Journal of Information and Communication Engineering, 1:3, 2005, Page 141-146

55 B. Liu, H. Cheng, J. Huang, J. Tian, J. Liu, and X. Tang, "Automated segmentation of ultrasonic breast lesions using statistical texture classification and active contour based on probability distance," *Ultrasound in medicine & biology,* vol. 35, pp. 1309-1324, 2009.

56 A. Madabhushi and D. N. Metaxas, "Combining low-, high-level and empirical domain knowledge for automated segmentation of ultrasonic breast lesions," IEEE transactions on medical imaging, vol. 22, pp. 155-169, 2003.

57 J. A. Noble, N. Navab, and H. Becher, "Ultrasonic image analysis and image-guided interventions," Interface focus, vol. 1, pp. 673-685, 2011.

58 P. Coupé, P. Hellier, C. Kervrann, and C. Barillot, "Nonlocal means-based speckle filtering for ultrasound images," IEEE transactions on image processing, vol. 18, pp. 2221-2229, 2009.

59 T. Loupas, W. McDicken, and P. Allan, "An adaptive weighted median filter for speckle suppression in medical ultrasonic images," IEEE transactions on Circuits and Systems, vol. 36, pp. 129-135, 1989.

60 C. Kervrann, J. Boulanger, and P. Coupé, "Bayesian non-local means filter, image redundancy and adaptive dictionaries for noise removal," in International Conference on Scale Space and Variational Methods in Computer Vision, 2007, pp. 520-532.

61 Zonderland H M, Coerkamp E G, Hermans J, van de Vijver M J and van Voorthuisen A E 1999 Diagnosis of breast cancer: contribution of ultrasound as an adjunct to mammography *Radiology* **213** 413–22

62 Huber S, Danes J, Zuna I, Teubner J, Medl M and Delorme S 2000 Relevance of sonographic B-mode criteria and computer aided ultrasonic tissue characterization in differential diagnosis of solid breast masses *Ultrasound Med. Biol.* **26** 1243–52

63 Dennis M, Parker S H, Klaus A J, Stavros A S, Kaske T I and Clark S B 2001 Breast biopsy avoidance: the value of normal mammograms and normal sonograms in the setting up of a lump *Radiology* **219** 186–91

64 Taylor K J, Merritt C, Piccoli C W, Schmidt R, Rouse G, Fornage B, Rubin E, Georgian-Smith D, Winsberg F,Goldberg B B and Mendelson E 2002 Ultrasound as a compliment to mammography and breast examination to characterize breast masses *Ultrasound Med. Biol.* **28** 19–26

65 Stavros T A, Thickman D, Rapp C L, Dennis M A, Parker S H and Sisney G A 1995 Solid breast nodules: use of sonography to distinguish between benign and malignant lesions *Radiology* **196** 123–34

66 . Garra B S, Krasner B H, Horii S C, Ascher S, Mun S K and Zeman R K 1993 Improving the distinction between benign and malignant breast lesions: the value of sonographic texture analysis *Ultrason. Imaging* **15** 267–85
67 . Donohue K D, Forsberg F, Piccoli C V and Goldberg B B 1999 Analysis and classification of tissue with scatterer structure templates *IEEE Trans. Ultrason. Ferroelectr. Freq. Control* **46** 300–10
68 . Georgiou G, Cohen F S, Piccoli CW, Forsberg F and Goldberg B B 2001 Tissue characterization using the continuous wavelet transform: II. Application on breast RF data *IEEE Trans.Ultrason. Ferroelectr. Freq. Control* **48** 364–73
69 . Shankar P M 2000 A general statistical model for ultrasonic scattering from tissues *IEEE Trans. UFFC* **47** 727–36
70 Shankar P M, Dumane V A, Reid J M, Genis V, Forsberg F, Piccoli C W and Goldberg B B 2001 Classification of ultrasonic B mode images of breast masses using Nakagami distribution *IEEE Trans. Ultrason. Ferroelectr. Freq. Control* **48** 569–80
71 . Shankar P M, Dumane V A, Piccoli CW, Reid JM, Forsberg F and Goldberg B B 2003 Computer-aided classification of breast masses in ultrasonic B scans using a multiparameter approach *IEEE Trans. Ultrason. Ferroelectr. Freq.Control* at press
72 . Kittler J M, Hatef R P, Duin W and Matas J 1998 On combining classifiers *IEEE Trans. PAMI* **20** 226–39
73 . E. Jakeman and P. N. Pusey, "A model for non-Rayleigh sea echo," *IEEE Transactions on Antennas and Propagation*, vol. 24, pp. 806-814, 1976.
74 . R. F. Wagner, S. W. Smith, J. M. Sandrik, and H. Lopez, "Statistics of speckle in ultrasound B-scans," *IEEE Transactions on Sonics and Ultrasonics*, vol. 30, pp. 156-163, 1983.
75 R. Barakat, "First-order statistics of combined random sinusoidal waves with applications to laser speckle patterns," *Optica Acta*, vol. 21, pp. 903-921, 1974.
76 . V. Dutt, "Statistical analysis of ultrasound echo envelope," Ph.D. dissertation, Mayo Graduate School, Rochester, MN, 1995
77. . R. Smolíková, "Neural and statistical modeling of ultrasound backscatter," Ph.D. dissertation, University of Louisville, Louisville, KY, 2002
78 . E. Jakeman, "On the statistics of K-distributed noise," *Journal of Physics A: Mathematical and General*, vol. 13, pp. 31-48, 1980.
79 . P. H. Tsui and C. C. Chang, "Imaging local scatterer concentrations by the Nakagami statistical model," *Ultrasound in Medicine & Biology*, vol. 33, pp. 608-619, 2007.
80 . T. Eltoft, "The Rician inverse Gaussian distribution: A new model for non-Rayleigh signal amplitude statistics," *IEEE Transactions on Image Processing*, vol. 14, pp. 1722-1735, 2005.
81 M. Martin-Fernandez, R. Cardenes, and C. Alberola-Lopez, "Parameter estimation of the homodyned K distribution based on signal to noise ratio," in *Proceedings of the IEEE Ultrasonics Symposium*, 2007, pp. 158-161.